Project 071 Predictive Simulation of nvPM Emissions in Aircraft Combustors

Georgia Institute of Technology

Project Lead Investigator

Suresh Menon
Professor at the School of Aerospace Engineering
Georgia Institute of Technology
270 Ferst Drive, Atlanta, GA 30332-0150
404-894-9126
suresh.menon@aerospace.gatech.edu

University Participants

Georgia Institute of Technology (GT)

- P.I.: Prof. Suresh Menon
- FAA Award Number: 13-C-AJFE-GIT-067
- Period of Performance: October 1, 2020, to September 30, 2025
- Tasks:
  1. Kinetic Modeling: Develop kinetic models to predict fuel decomposition and soot precursor polycyclic aromatic hydrocarbon (PAH) pathways in representative sooting fuels
  2. Nucleation Modeling: Develop reduced incipient particle nucleation rates according to PAH dimerization rates from molecular dynamics (MD) simulations
  3. Surface Growth and Aggregation Modeling: Develop a blended reaction-transport-limited growth model of soot particle aggregation
  4. Large eddy simulation (LES) of soot formation within canonical flames, strategy to upscale the soot formation to resolve LES scales, integrate the updated rates in the global soot models, and apply them to predict soot formation in complex rich-quench-lean configuration

Project Funding Level

The current project was funded initially for a 3-year effort (July 2020 to September 2023), with a request of $500,000 per year from ASCENT (per year). An additional request for no-cost extension was approved for the remainder of the term till September 2025. Cost-sharing is provided as follows.

- GT provides cost-sharing for its share of $150,000 per year. The GT point of contact (POC) is Kevin Ellis (kevin.ellis@aerospace.gatech.edu).
- Raytheon Technologies Research Center (RTRC) provided cost-sharing of $250,000 per year. Dr. Colket is a consultant on this project with many years of experience in soot modeling. The RTRC POC is John LaSpada (LaSpadJW@RTRC.utc.com).
- University of Michigan (UM) provides cost-sharing in the amount of $100,000 per year. The UM POC is Alexandra Thebaud (thealexi@umich.edu).

Investigation Team

Georgia Institute of Technology

Prof. Suresh Menon, GT: (P.I.), Task 4
Mr. Shubham Karpe, GT: (Student), Task 4

Raytheon Technologies Research Center

Dr. Miad Yazdani, (co-P.I.), Task 3
Dr. Steve Zeppieri, (co-P.I.), Task 1
Dr. Meredith Colket, (co-investigator), Task 3

University of Michigan
Prof. Angela Violi, (co-P.I.), Task 2

Project Overview

This project aimed to establish a new multiscale framework for predicting soot formation in both canonical and practically relevant sooting flames. A hierarchy of first-principles simulation methods was employed to capture the multiscale physics governing the formation and transport of non-volatile particulate matter (nvPM, commonly referred to as soot). The work specifically targeted several empirical elements that traditionally limit soot modeling fidelity, for example, uncertainties in particle inception models, the roles of key precursor species in nucleation, assumptions regarding particle morphology and their effects on surface growth, sensitivities to particle size distribution, and the use of ad hoc coagulation and coalescence formulations. To address these challenges, the state-of-the-art modeling tools are developed and a systematic coupling of these tools in a multiscale, multiphysics manner is established. Hence, this approach provides insights into establishing new predictive abilities by integrating these capabilities. The final objective of this work demonstrated the capabilities of this approach to modeling the soot physics in realistic gas turbine combustor for which the experiments are being conducted under Federal Aviation Administration (FAA) ASCENT Project 070.

The multiscale and multiphysics layers of collaborations among the cost-sharing groups are summarized in Figure 1 and Figure 2 and briefly described herein. In Year 1 and 2 efforts, at Georgia Tech, the method of moment-based soot model is first established using canonical studies of ethylene fuels and key inputs for improvements are identified by investigating the sensitivity of soot predictions to different modeling components. These conditions are then provided to other collaborative groups for establishing their modeling approaches. Specifically, the kinetics group at RTRC compared different gas-phase kinetics in predicting important soot precursor species. These efforts primarily resulted in the development of detailed gas-phase kinetic mechanism that was provided to UM. In the UM study, the propensity of gas-phase species to form dimers (considered the building blocks of soot inception) under flame conditions was studied using MD simulations. A unique approach based on machine learning was developed that can be potentially extended to any relevant sooting fuel to obtain the inception rates that can be provided to post-inception growth modeling. At RTRC, Monte Carlo (MC) simulations approach was established using jet-fueled lean direct injection (LDI) combustor data simulated at GT to understand the fractal growth of soot aggregates. At Georgia Tech, the modular moment-based soot modeling was established to assemble the above inputs it. Additionally, standalone linear eddy mixing (LEM-MOM) approach was established to upscale the soot source rates at LES level scales.

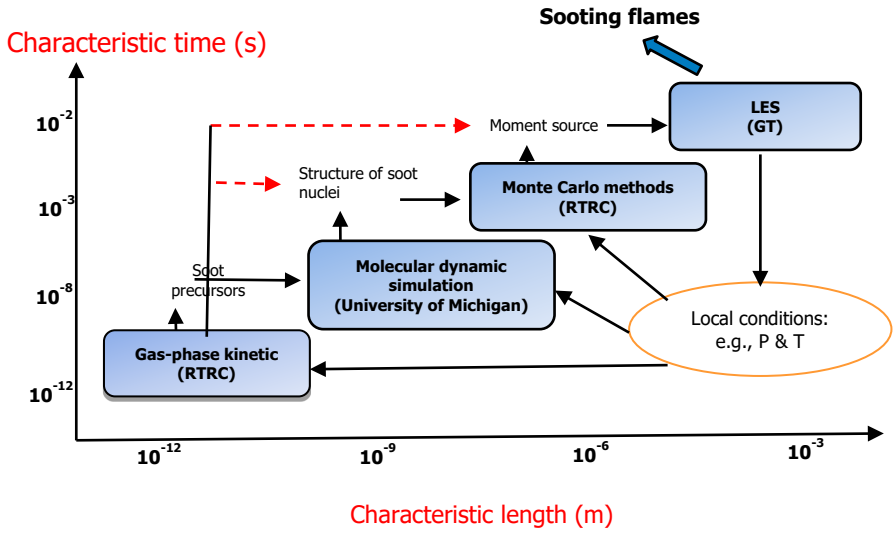

Figure 1. Multiscale collaborative efforts to improve non-volatile particulate matter (nvPM; soot) predictions. LES: large eddy simulation, GT: Georgia Institute of Technology, RTRC: Raytheon Technologies Research Center.

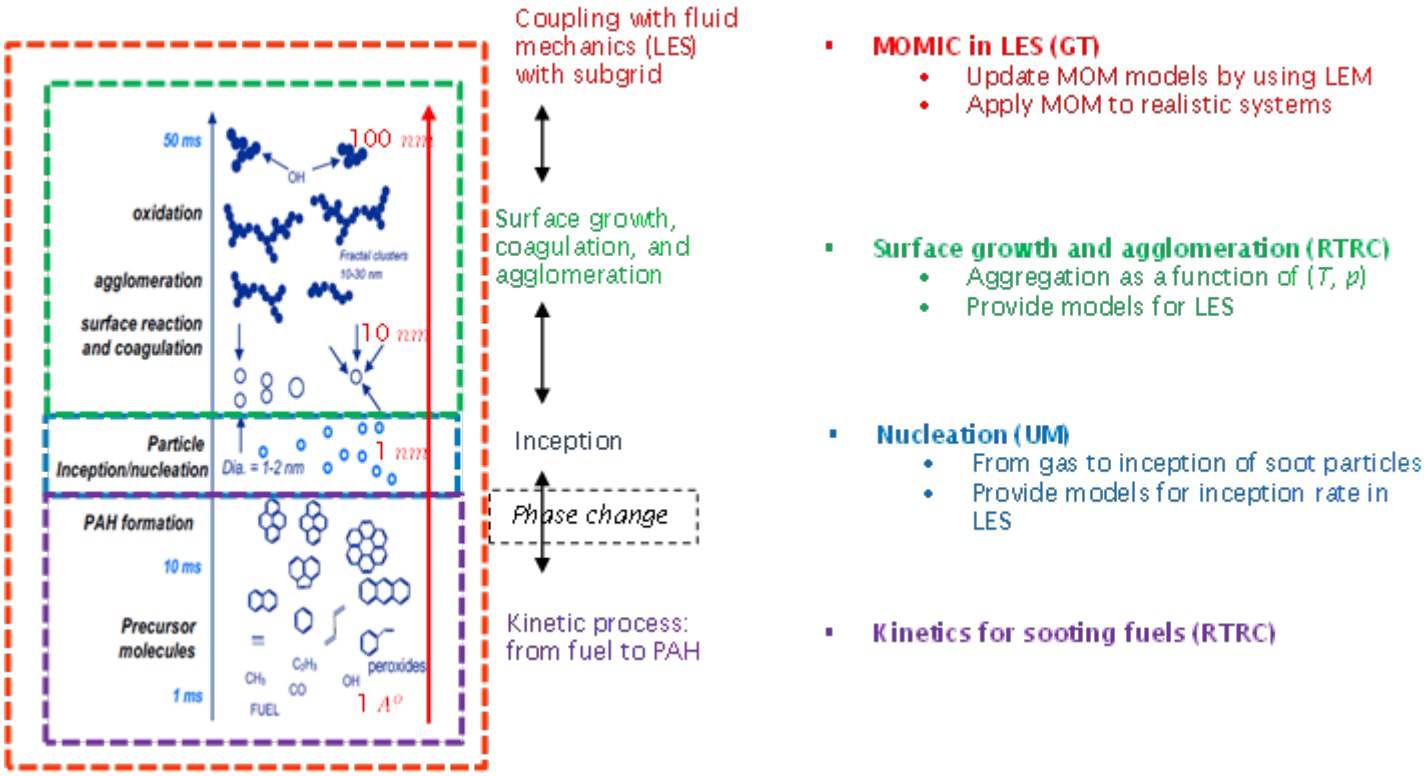

Figure 2. Multiscale collaborative efforts to improve non-volatile particulate matter (nvPM; soot) predictions. LES: large eddy simulation, GT: Georgia Institute of Technology, MOMIC: method of moments with interpolative closure, PAH: polyaromatic hydrocarbons, RTRC: Raytheon Technologies Research Center, UM: University of Michigan.

In the Year-3 and NCE efforts, this established collaborative approach is extended to study soot evolution in a realistic single sector Rich-Burn Quick-Mix Lean-Burn (RQL) model combustor operated using conventional jet fuels. At first, LES studies at GT conducted non-sooting simulations of this rig to generate a useful parametric space as representative conditions to be used in different modeling components of the collaborative partners. The kinetics activities at RTRC resulted in the development of a 210-species detailed mechanism with formation of PAH species till five aromatic rings. The molecular dynamics-based studies identified key soot precursors and the rates of formation of soot nuclei under RQL combustion-relevant conditions and formed a semi-empirical modified expression of soot nucleation using benzopyrene (A_4R_5). This nucleation rate was provided to GT to update the source terms associated with nucleation processes in the method of moment-based soot model, and the information on the structures of these soot nuclei was also provided to RTRC for modeling surface growth and aggregation processes along the streamlines of RQL combustor. At GT, LES studies soot formation from RQL combustor under two operating conditions were performed using a reduced gas-phase kinetic mechanism with PAH formation pathways till naphthalene. Due to the heavy computational cost incurred during the simulations even with the reduced gas-phase kinetics, the coupled soot model inputs were not directly used in the LES. Rather using the baseline LES data, a predictive computational fluid dynamics (CFD)-Chemical Reactor Network (CRN) strategy was adopted to construct a reduced reactor network model and is then used to understand the relative effects of incorporating detailed kinetics and inception model obtained as inputs from multi-scale collaborative studies.

Task 1 – Kinetic Modeling

Raytheon Technologies Research Center

Objective

The objective of this task is to develop a chemical kinetic model of parent fuel decomposition and oxidation reactions, with a special focus on fuel rich chemistry, to enable the accurate evolution of PAH/soot precursor formation and incipient soot particle formation.

Milestone(s)

- Develop a detailed kinetic mechanism with PAH pathways for ethylene and jet fuels.
- Formulate a semi-empirical soot model for coupling with CFD.

Research Approach

The schematic in Figure 3 shows the coupling among the LES, nucleation, and kinetic activities focused on during this project, where T, P, and ϕ represent the temperature, pressure, and equivalence ratio of the surrounding gas phase, respectively. For ethylene fuels, the conditions corresponding to well-stirred reactors (Brown et al., 1998), laminar premixed flames in international sooting flame workshop were used as a baseline, whereas for the jet fuels, the non-sooting simulations conducted using LES were used to map the local ranges of conditions witnessed in the combustor. Based on the developed gas phase kinetics, information about the key precursor PAH species is passed to the nucleation modeling activities at university of Michigan and the detailed kinetics is provided to GT.

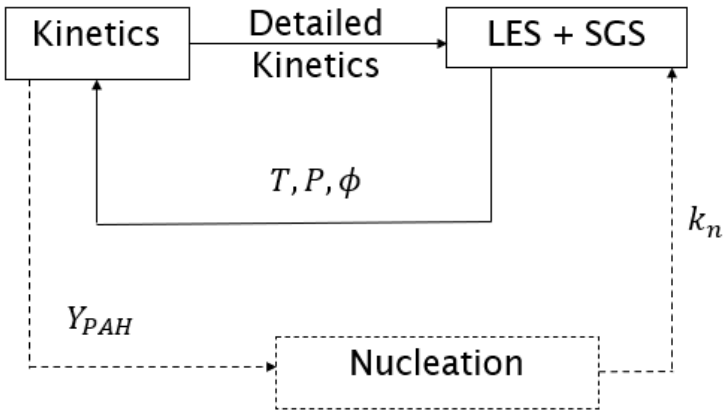

Figure 3. Coupling of large eddy simulation (LES)–kinetic activities. PAH: polyaromatic hydrocarbon, SGS: subgrid-scale.

The Year 1 activities mainly focused on kinetic model development of ethylene fuel to establish the methodology. The set of detailed chemical mechanisms at GT were extended here to include a comprehensive list as below: Appel-Bockhorn-Frenklach (101 species/544 reactions), Wang-Frenklach (99 species/533 reactions), National Jet Fuels Combustion Program (NJFCP) Foundational Chemistry sub model with Strategic Environmental Research and Development Program (SERDP) PAH reactions (166 species/504 reactions), NJFCP Foundational Chemistry sub model with King Abdullah University of Science and Technology (KAUST) PAH reactions (168 species/818 reactions), Full ARAMCO®-KAUST C_4 mechanism (581 species/3,037 reactions), CRECK Natural Gas mechanism (114 species/1,999 reactions), University of Connecticut (UCONN) (Lu) Skeletal ethylene (C_2H_4) mechanism (33 species/206 reactions). The Lu skeletal mechanism serves as a proxy for the reduced 19 species ethylene mechanism currently used at GT, because both mechanisms derive from the same fully detailed mechanism. These models were benchmarked against published ethylene datasets for comparative analysis against both experimental data and relative performance against the various models.

® ARAMCO is a registered trademark of Saudi Arabian Oil Company, Dhahran, Saudi Arabia.

The skeletal mechanism from T. Lu has been used to optimize the global soot kinetic model. The Lindstedt 4-step soot model consists of nucleation step based on acetylene (C_2H_2) precursor, soot surface growths based on C_2H_2, soot oxidation via hydroxide (OH) and dioxygen (O_2). The perfectly stirred reactor (PSR) studies are conducted using Chemkin® to optimize the coefficient [pre-exponential factor, minimum C atoms to form soot nuclei, Activation energy (E_a/R)] to develop a new soot kinetic model. Th results of soot evolution with PSR studies for a wide range of temperature conditions, using the Lindstedt soot model, method of moments in Chemkin and the improved kinetic model are demonstrated in Figure 4a. The improved kinetic model can predict trends very well (specifically the reduced rates and soot mass fractions at elevated temperature) consistent with Chemkin Method of Moments (MOM), as opposed to Lindstedt model. The updated model is also coupled with other detailed kinetics to predict the variations in soot mass fractions and results are displayed in Figure 4b. It can be seen that predictions of soot mass fractions from the updated soot kinetics coupled with different mechanisms are consistent. The small discrepancy lies with the uncertainty in predictions of C_2H_2 mass fractions which acts as soot precursor.

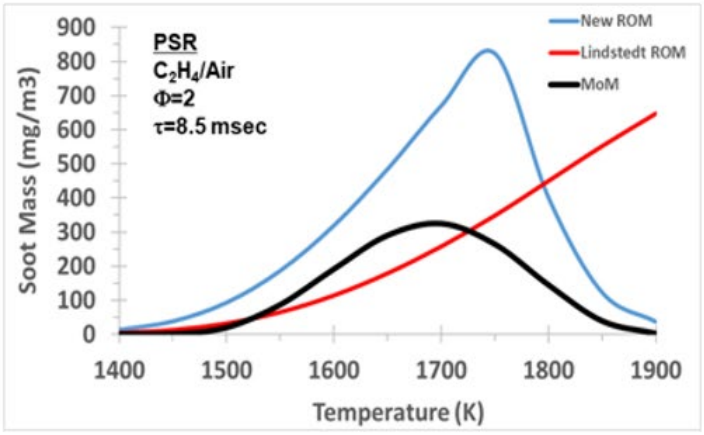

(a) Improved soot kinetic over range of temperature

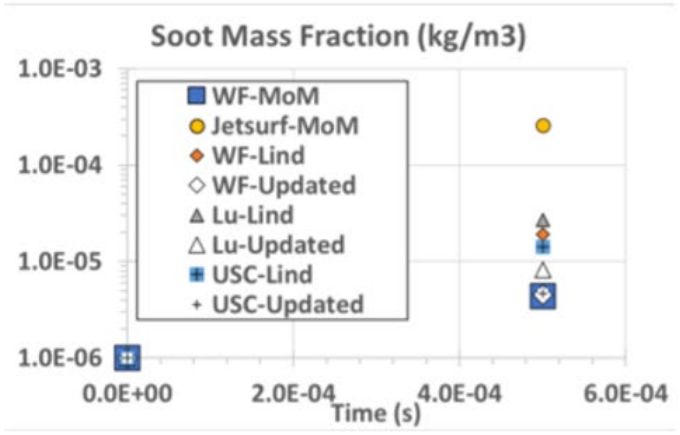

(b) Updated soot kinetic model with detailed mechanisms

Figure 4. Assessment of the improved soot kinetic model at Raytheon Technologies Research Center (RTRC). MOM: Method of Moments, PSR: perfectly stirred reactor.

The later efforts were focused on the completion and assessment of chemical kinetics models coupled to PAH formation for logistic (Jet-A) fuels. In summary, the HyChem (Hybrid Chemistry) (Wang et al., 2018) method was used, in which semi-empirical reactions treat the parent fuel decomposition process to the relevant intermediate hydrocarbon species, and the so-called SERDP technique, in which compositions of several surrogate hydrocarbon species are formulated that capture the bulk properties of the fuel of interest (for example, Jet-A fuel would be considered a binary blend of *n*-dodecane and *m*-xylene). The HyChem model was coupled with both the SERDP and KAUST PAH-chemistry (Selvaraj et al., 2016) models for analysis and the SERDP model was coupled with the SERDP PAH-chemistry model. Finally, the California Institute of Technology (Caltech)-mech (Blanquart et al., 2009) model was appended with the HyChem model to incorporate additional reactions related to the decomposition of Jet-A fuels. The overall layout of the workflow adopted in this effort is highlighted in Figure 5. This assessment is carried out using a perfectly stirred reactor configuration where a mixture of Jet-A (assumed as 77% nC12, 23% *m*-xylene)/air is subjected to the following conditions *P*: 1-5.8 atm, τ_{res}: 1-25 msec, ϕ : 0.5–5.5, T: 1,400–2,300K which were based on local conditions obtained from non-sooting simulations of RQL combustor at GT.

® Chemkin is a registered trademark of Ansys, Inc., Canonsburg, Pennsylvania.

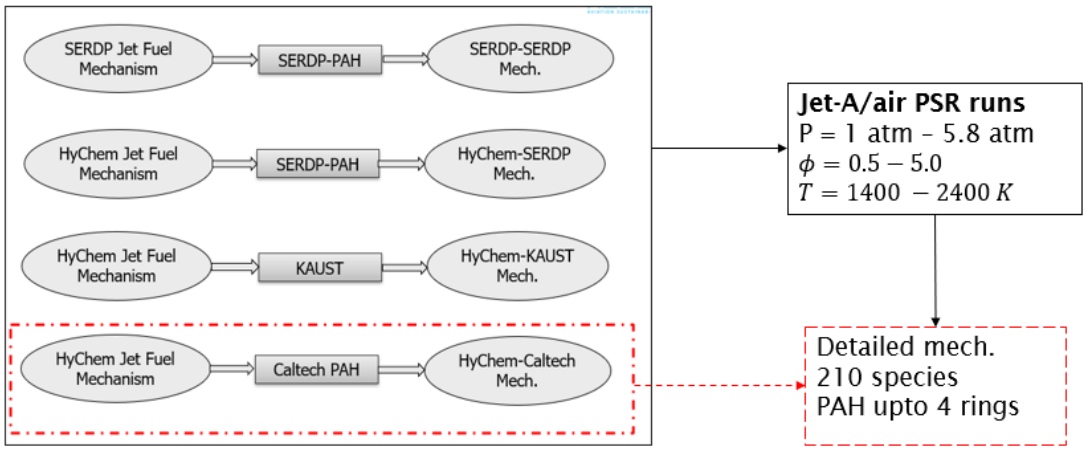

Figure 5. Assessment of detailed gas-phase chemical mechanisms, the red dashes depict the final delivered gas phase kinetics through Raytheon Technologies Research Center (RTRC) kinetic activities. PAH: polyaromatic hydrocarbon, PSR: perfectly stirred reactor.

The key outcomes of kinetic activities are discussed briefly here. The results obtained from the assessment of all detailed gas phase mechanisms are provided in Figure 6. As can be seen from Figure 6a, overall predictions of temperature are similar for all mechanisms. Some visible differences arise in the range of higher equivalence ratios. The benzene (C_6H_6) profiles and acetylene (C_2H_2) profiles are in qualitative agreement among mechanisms except the Pitsch mechanism (Langer et al., 2023), which must be investigated further. Encouragingly, both the HyChem models and the Caltech-mech model have an overall satisfactory agreement.

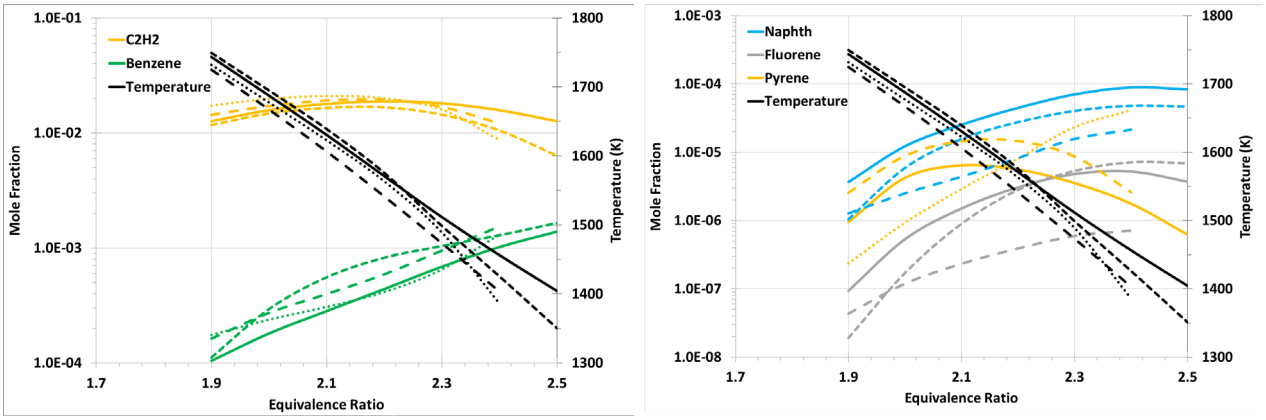

(a) Comparison of major precursor species (b) Comparison of heavier PAH species

Solid:	**Caltech Mech**
Dash:	**Pitsch et al.**
Dot:	**Hychem/Kaust Mech.**
Long Dash:	**Hychem/SERDP Mech.**

Figure 6. Assessments of key soot relevant characteristics among different detailed mechanisms.

The nucleation studies at UM required addressing the formation of heavier PAH species which play a critical role in the inception of soot particles. In this regard, a comparison of major PAH species that are used in the state-of-the-art nucleation models was conducted across a range of conditions. Such an assessment for key species such as naphthalene ($C_{10}H_8$), fluorene ($C_{13}H_{10}$), and pyrene ($C_{16}H_{10}$) is provided in Figure 6b. The results suggest a wider spread of PAH species among all four mechanisms that may be crucial in predicting the early nucleation stages of soot formation in large-scale simulations. The Pitsch mechanism was relatively new and required further assessment. Keeping this in mind, further analysis is presented here for comparing predictions of soot formation for ethene using Wang-Frenklach, HyChem-KAUST, HyChem-SERDP and Caltech-mech with particulate matter reduced order model (PM-ROM) model (optimized rates for Lindstedt soot model) described earlier. The RTRC formulation extends the original premise by adding benzene as key PM forming species, the hydroxyl radical as another oxidation species and the utilizes a double Arrhenius rate expression for both the inception and surface growth processes that enables the model to capture the well-known and experimentally observed "soot bell" concentration profile with respect to temperature.

Figure 7 suggests that the soot concentration levels at range of temperature from Wang-Frenklach, HyChem SERDP and Caltech-mech show similar behavior in terms of bell-shaped dependency on temperature. The HyChem-KAUST predictions are qualitatively very different compared to the other three mechanisms. In terms of quantitative analysis, HyChem-SERDP mechanism underpredicts soot levels by a factor of 1.5 at higher equivalence ratios than Wang-Frenklach mechanism. Similarly, the Caltech-mech overpredicts soot levels by a factor of 1.5-2 when its predictions are compared with Wang-Frenklach mechanism.

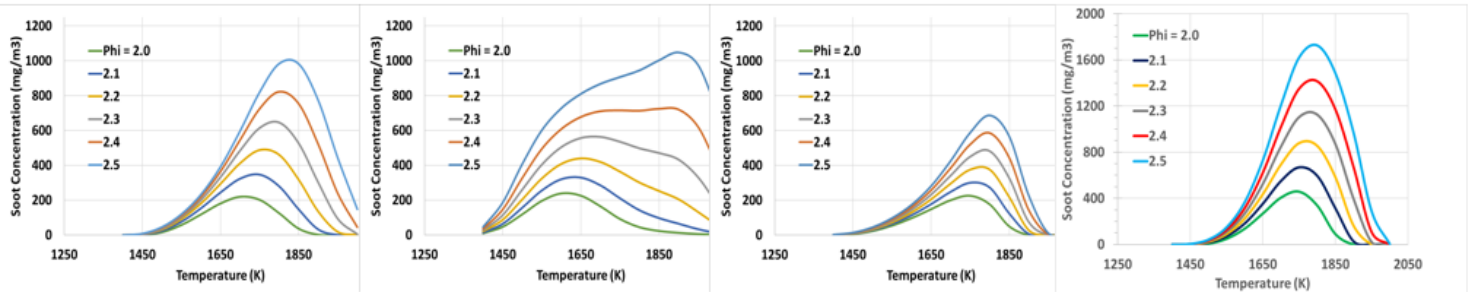

Figure 7. Comparison of soot volume fractions for different gas phase mechanisms: WF, HyChem-KAUST, HyChem-SERDP, Caltech-mech from left to right.

In the next set of activities, predictions are compared by changing the fuel to Jet-A fuels under the same operating conditions investigated for ethene fuels mentioned above. The HyChem-KAUST, HyChem-SERDP and Caltech-mech mechanisms are assessed against each other. As can be seen from Figure 8, the predictions from Caltech-mech and HyChem-KAUST agree with each other quantitatively. However, HyChem-KAUST predicts two peaks in soot levels whereas Caltech-mech predicts only one peak and bell-shaped dependency. This qualitative bell shaped one peak trend is also visible in the predictions of HyChem-SERDP; however, the quantitative magnitude is factor of 3 lower than Caltech-mech and HyChem-KAUST mechanism.

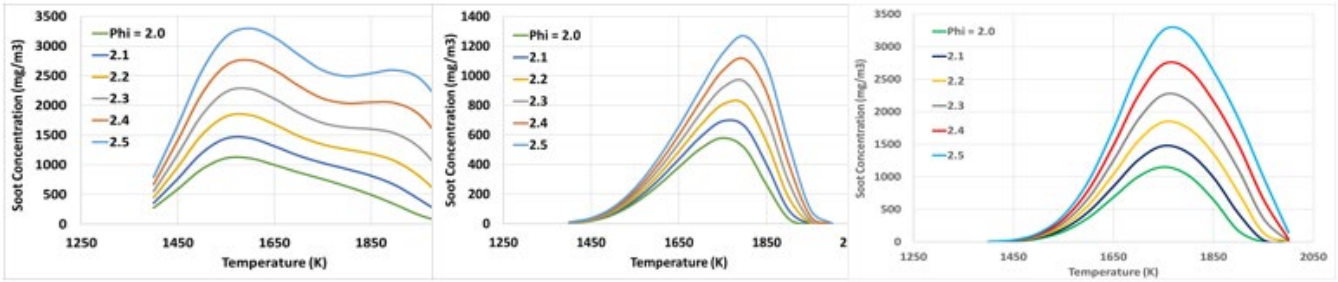

Figure 8. Comparison of soot volume fractions for different gas phase mechanisms: HyChem-KAUST, HyChem-SERDP, Caltech-mech from left to right.

With the analysis of the ethene/air and Jet-A/air simulations combined for the same reactor conditions, considering the trends as well as quantitative levels of soot predictions, Caltech-mech seems to be the best mechanism and is used to derive the final 210 species detailed mechanism, provided later to GT and UM for their modeling activities.

Finally, to conclude upon the final piece of kinetic activities at RTRC, the PM-ROM model is further optimized of rates for the Lindstedt soot model with the newly developed 210 species detailed mechanism. "Soot bell" concentration profile with respect to temperature. As the objective was to generate a higher fidelity PM-ROM model, a numerical shooting fitting procedure was used to establish rate coefficients that enabled the PM-ROM model to identically match the soot concentration levels generated via detailed kinetic analysis coupled with moment-based soot calculations. In the most recently developed PM-ROM, the reduced model was calibrated against PSR calculations at the elevated pressure (5.8 atm) and air temperature (600K) conditions of RQL combustor operation. The nominal reactor residence time for these calculations was 5 ms, and the fuel-air equivalence ratio spanned from 1.8 to 2.5. The detailed mechanism used was the previously discussed HyChem-Caltech mechanism. The agreement between the soot concentrations generated via detailed kinetics and MOM and the PM-ROM are shown in Figure 9, indicating quite good agreement.

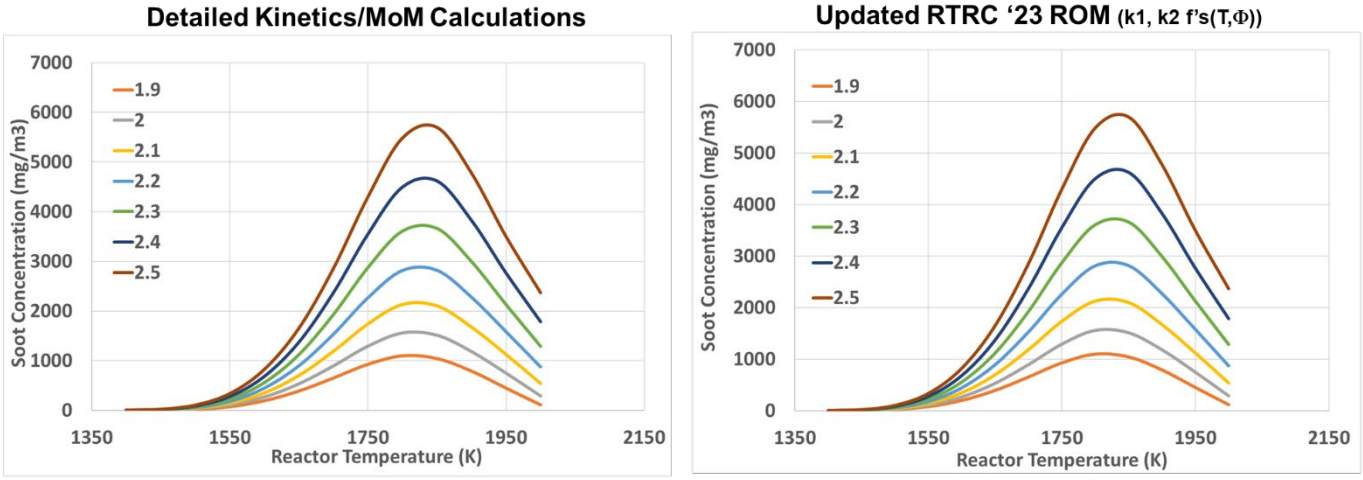

Figure 9. Comparison of soot concentrations generated from the two modeling approaches listed at nominal rich-burn quick-mix lean-burn (RQL) combustor conditions. MOM: method of moments, PSR: perfectly stirred reactor, PM-ROM: , RTRC: Raytheon Technologies Research Center.

Recognizing that two-dimensional (2D) (i.e., temperature and equivalence ratio) correlation may not be computationally efficient, the developed rate correlations were reduced to one-dimensional (1D) as follows. The developed rate expression equivalence ratio dependencies were averaged over the range, yielded rate constants that were functions only of temperature. The average rate expressions for nucleation and surface growth processes are shown in Figure 10.

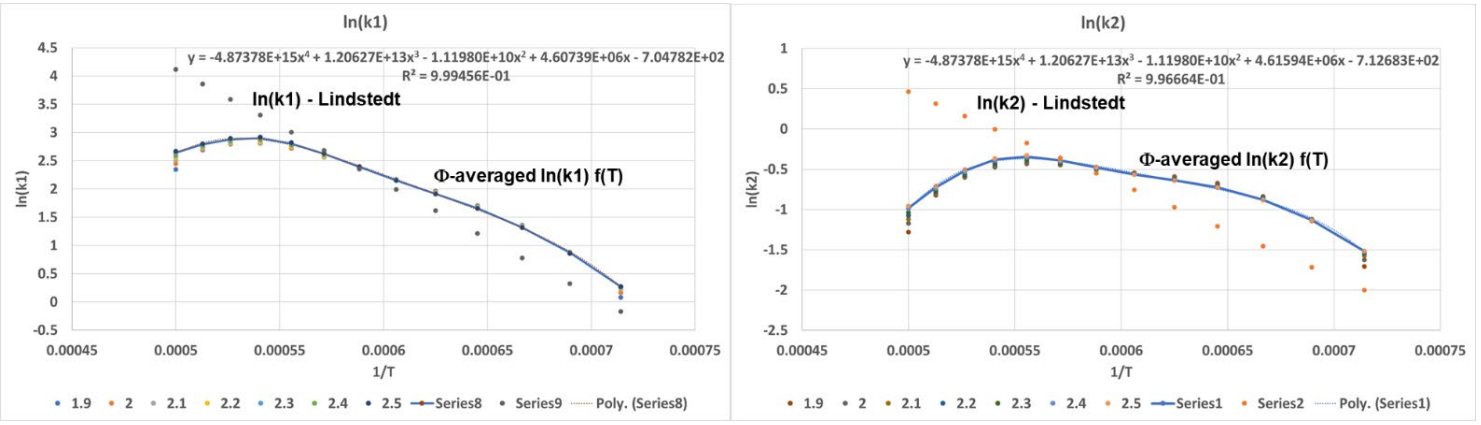

Figure 10. Fuel-air mixture averaged kinetic rate expressions for nucleation (Left) and surface growth (Right) for use in the PM-ROM Tool.

With this new temperature only rate expression, the soot concentration outputs associated with the PSR simulations were then computed and compared against the original detailed chemistry/MOM calculations. This comparison is shown in Figure 11. As can be seen in Figure 11, there is a slight decrease and slight increase in the fuel rich and lean, respectively, conditions, but overall, the concentration values are in good agreement with the detailed data.

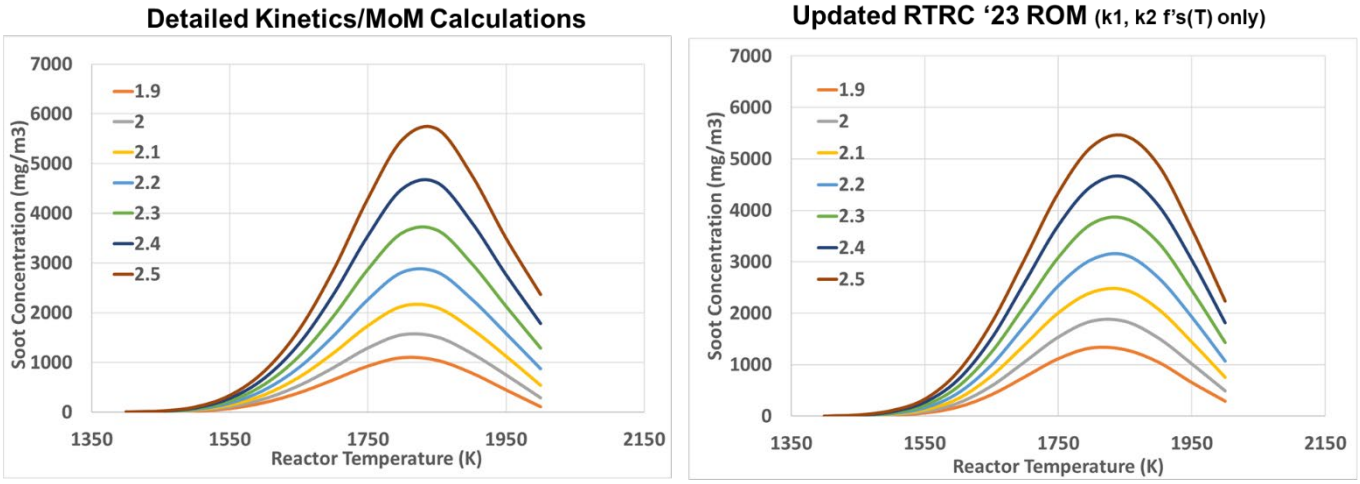

PSR Settings: Jet-A/Air, P: 5.8 atm, τ_{res}: ~5 msec, Φ: 1.9-2.5, Air Inlet T: 600 K, Reactor Temp's: 1400-2000 K

Figure 11. Comparison of soot concentrations generated from the two modeling approaches listed at nominal rich-burn quick-mix lean-burn (RQL) combustor conditions. MOM: Method of Moments, PSR: perfectly stirred reactor, PM-ROM: RTRC: Raytheon Technologies Research Center.

Major Accomplishments

- Developed a detailed jet-fuel kinetic mechanism (210 species) and delivered to GT.
- Formulated a two-equation, four-step PM-ROM soot model as an improvement over the Lindstedt model, enabling closer agreement with detailed MOM-based predictions.

Publications
None.

Outreach Efforts
None.

Awards
None.

Student Involvement
None.

Plans for Next Period
None.

Task 2 – Nucleation Modeling
University of Michigan

Objective
The objective of this task is to develop models for nanoparticle inception, a critical step in predicting emissions. This effort bridges the work on gas-phase chemistry (RTRC) with the model for particle growth (RTRC) and provides inputs for the moment model (GT) and growth models (RTRC) using atomistic simulations.

Milestone(s)
- Developed a reduced nanoparticle inception model based on dimerization of PAH species.

Research Approach
Current models for particle inception are unable to reproduce a variety of experimental data, including molecular structure. This work aims at developing a predictive model for particle inception that can provide accurate chemical and physical growth pathways for PAHs. Molecular dynamics simulations are used to study the collisions of PAHs and the formation of aromatic dimers leading to soot inception. These atomistic simulations coupled with advanced sampling techniques are used to study the collisions of PAHs.

Free energy calculations provide information on the effect of chemical structure and shape on the tendency to form nuclei. After collaboration with RTRC, PAHs that are critical to inception are identified. A pool of aromatic compounds such as pyrene, benzopyrene, coronene, ovalene, circumcoronene are selected. Initially, some preliminary studies for free energy calculations are conducted at temperatures of 500K and 1,000K. As can be seen from Figure 12, at lower temperatures all PAHs seem to be forming dimers even though it is more favorable for higher PAHs to form a dimer. However, at higher temperature of 1,000K (typical of flame temperature conditions), only higher PAHs have tendency to form dimers. This suggests nucleation model from traditional pyrene precursors fails to participate in the actual soot inception processes.

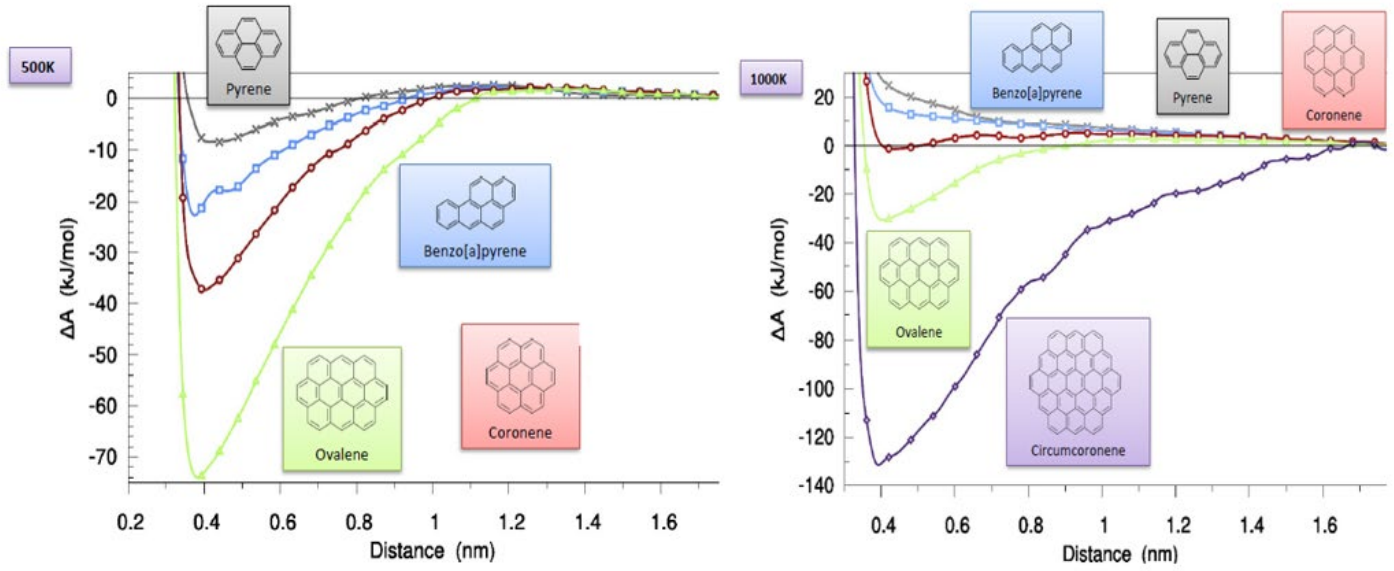

Figure 12. Free Energy calculations of polycyclic aromatic hydrocarbons (PAHs) as function of temperature.

The initial pool of PAH species is later extended to include atomistic simulations of higher PAH species that also include oxygen. Figure 13 shows the structures of gas-phase compounds considered in this study and the results for their homo-dimerization propensity. The data points are broadly clustered in three groups. The first, composed of compounds I.C (462 u), I.D (462 u), and I.E (460 u), which have the same mass and O/C ratios (0.125), and are less stable than I.A (448 u) and I.B (472 u), which constitute the second group. This difference indicates that the presence of oxygen slightly destabilizes the dimers, an effect possibly caused by the increased repulsive electrostatic interactions of oxygenated molecules compared to pure aromatic hydrocarbons. The third group is formed by I.F (402 u), I.G (452 u), and I.H (502 u), which are less likely to dimerize than the other two groups. The low dimer stability of the third group can be due to the presence of a sigma bond, which introduces an internal rotatable bond that interferes with the formation of clusters. A few points can be drawn from this study. First, the details of the structure of the species that nucleate cannot be ignored. It has been suggested that the mounting evidence of the presence of five-membered rings, aliphatic side chains, and oxygenated groups in soot precursors, does not change the nucleation mechanism that leads to soot formation. Our results, both pertaining to the dimerization propensity and the change in free energy barriers between monomers and dimers, which directly relates to the kinetic rates of dimerization, show otherwise. Second, the effects of shape, presence of oxygen, mass, and rotatable bonds are tightly intertwined, and have different importance as well as diverse temperature dependencies, although, they are all dominated by entropic effects at high temperatures. The presence of oxygen affects the dimer propensity, by reducing the molecular cohesion due to electrostatic repulsion although, it should be noted that the force field employed in this study cannot capture the effect of molecular polarizability.

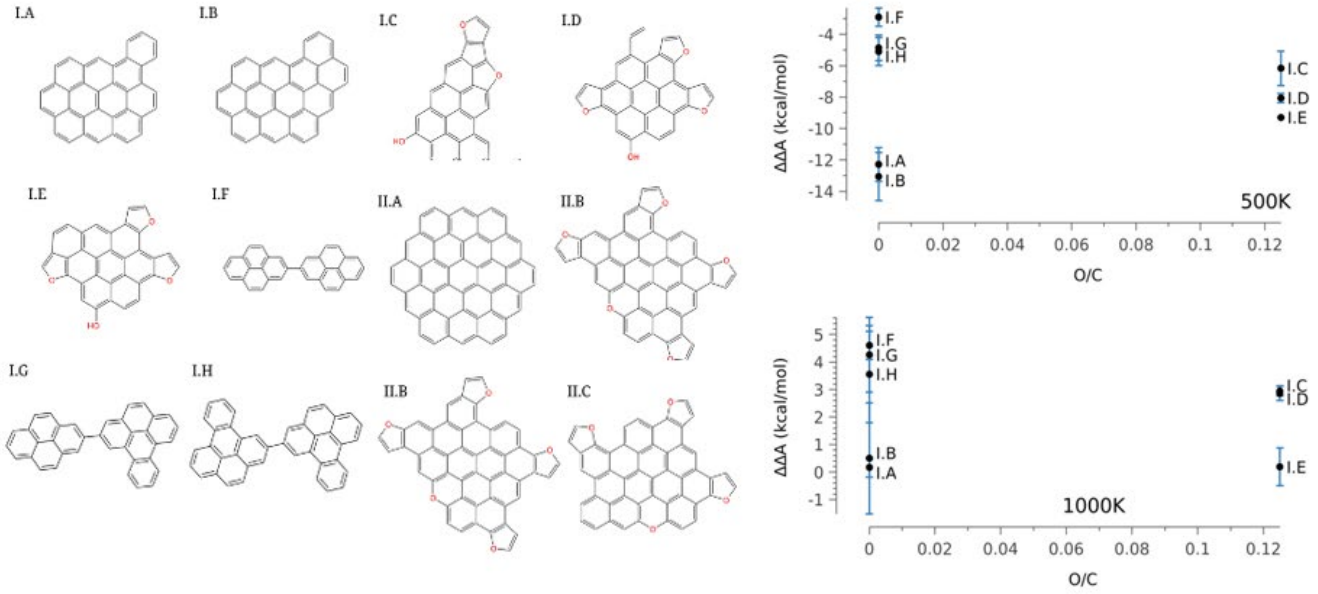

Figure 13. Structural formula of gas-phase compounds (left) and homo-dimerization propensity at 500K and 1,000K as a function of their oxygen/carbon ratio.

In the next task, we focused on machine learning algorithms with the goal of leveraging this technique to predict dimerization propensity of various polycyclic aromatic compounds (PAC). While molecular dynamics simulations can provide this information for specific dimer pairs, it is not feasible to extend this to all potential dimer components. With millions of different PACs observed in even simple flames, it is too costly to compute this information for all possible PACs, especially when accounting for the combinations of hetero dimerization between different PAC molecules. Recently, machine learning has shown potential to learn complex quantitative relationships between PAC properties and predict the energy difference between the monomer and dimer state for an arbitrary pair of PACs with minimal computational cost. However, the approach only considered thermodynamic energy differences at a single temperature and therefore is insufficient to predict the energy barriers needed to derive kinetic rates.

As a first step, we perform numerous Meta dynamics molecular dynamics simulations to calculate the dimer energy barrier for a large dataset of PACs at multiple temperatures. This value is critical in characterizing the kinetic stability of the PAC dimer, and in conjunction with equilibrium data can provide a comprehensive description of forward and reverse barriers and rates in the dimerization process. Molecular dynamics simulations enhanced by Meta dynamics were used to reproduce the free energy landscape of the dimerization process as a function of the center-of-mass (COM) distance. To define the chemical space, a wide set of PACs was considered, as reported in the last report, which broadly reproduces the sizes, shapes, and functional groups observed in flame systems. In order to describe PAC chemistry, we compute a set of 312 descriptors for each molecule. These descriptors capture properties such as mass, atomic ratios such as carbon-hydrogen ratio, and counts of specific subgroups such as aromatic rings. From our simulations, we obtain 315 unique energy barriers between the monomer and dimer states. Generally, we observe the same qualitative relationships with size and temperature. All else being equal, free energy barriers tend to increase with mass as Van der Waal's and electrostatic interactions become stronger and decrease with temperature as entropic effects increase in importance. It is important to note, however, that these two parameters are insufficient to describe all differences observed in the energy barrier and a quantitative trend cannot accurately be derived solely from these two values. Different machine learning (ML) algorithms were explored while still running molecular dynamic simulations. Figure 14 below shows our target ML algorithm.

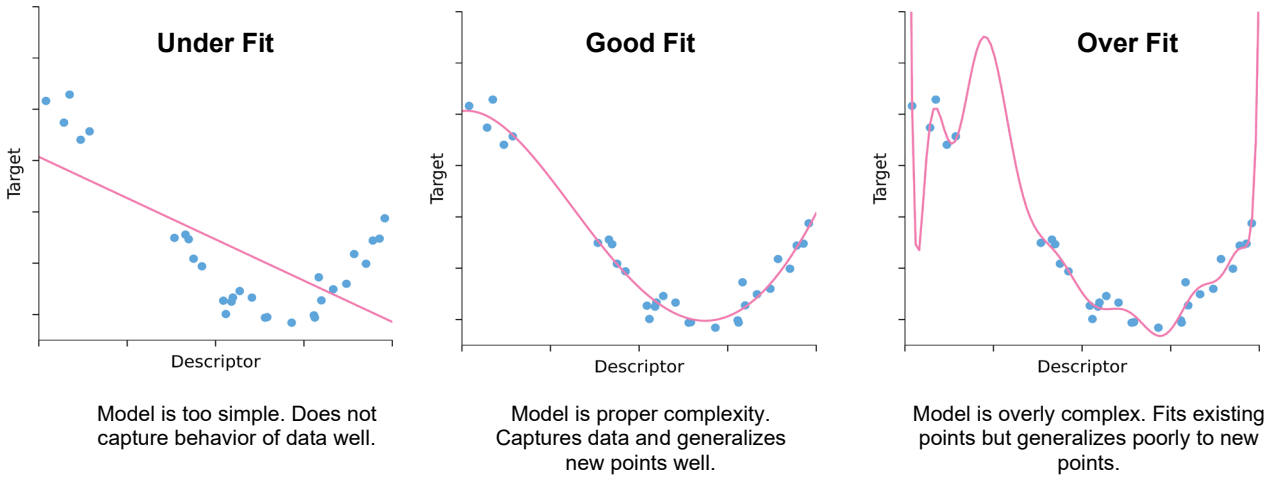

Figure 14. Evaluation of machine learning algorithms.

In order to analyze the complex space, we resort to machine learning with good fit models. Before training our machine learning model, we eliminated similar features by removing any feature with a variance of zero and any feature with a Pearson correlation greater than 0.95. To build a predictive model for the formation efficiency (FE) of aggregation, we applied the Lasso method as it allows for high accuracy and often interpretable predictions. Lasso is a supervised machine learning regression model that minimizes a loss function. It uses the least absolute shrinkage and selection operator, has been applied successfully to make interpretable pre-dictions in chemical problems as it eliminates extraneous features and only selects a smaller sub-set of properties needed to make predictions.

Our model outperforms existing physical dimerization models present in the literature. We compared our results, including the test on a restricted dataset with no data leakage, with three additional models. One advantage of Lasso is its ability to provide a degree of interpretability towards the aspects that control prediction, as it sets coefficients of unused features to zero. Thus, by analyzing which features the Lasso model retains, we can gain a sense of which molecular properties are important for predicting the FE of dimer aggregation. Of note, while some of the molecular properties discussed below resemble quantities that have been used in the past to predict the aggregation propensity, they are not generally interchangeable with those found in literature. Overall, across all 105 folds of cross validations, the model selects a nearly identical set of 10 features. If we exclude these top features, no other feature is selected in more than four folds and as such we will not discuss them. Broadly, the top features can be divided into three groups of properties that are important for PAC dimerization: size, shape, and presence of specific chemical groups.

The first class of properties are extrinsic properties that are broadly related to the size of the molecule. Specifically, the algorithm selected the number of aromatic rings, the number of carbons not connected to a hydrogen, the number of tessellations containing four carbons, the number of tessellations with three carbons and a hydrogen, and the number of six-membered rings. Figure 15 below shows that the FE of dimerization is strongly related to the (harmonic) average number of aromatic rings in the dimer (Pearson coefficient of −0.8397 and Spearman coefficient of 0.8719). This result agrees with the general observation that PACs will often cluster in lateral stacks, and the interaction strength between PACs is closely related to their number of aromatic rings. Among the molecular descriptors in this class, the number of aromatic rings is the feature that has the highest correlation with the FE (more than the number of six membered rings, for example), but it is crucial to note that, by itself, it is not sufficient to fully capture the physical dimerization. A linear fit of the FE as a function of the total number of aromatic rings produces predictions model with a root mean square error (RMSE) of 15.6 kJ mol−1 and a mean absolute error (MAE) of 11.3 kJ mol−1, which has a significantly larger error than our model and is (not coincidentally) comparable to using only the mass as a descriptor. Some features in this group encode size with molecular shape information. One such example is the number of internal carbon atoms, defined as the aromatic carbon atoms that are not bonded to H atoms. As most of the molecules in the dataset are highly peri condensed hydrocarbons, these PACs will have a greater percentage of internal carbons than catacondensed PACs.

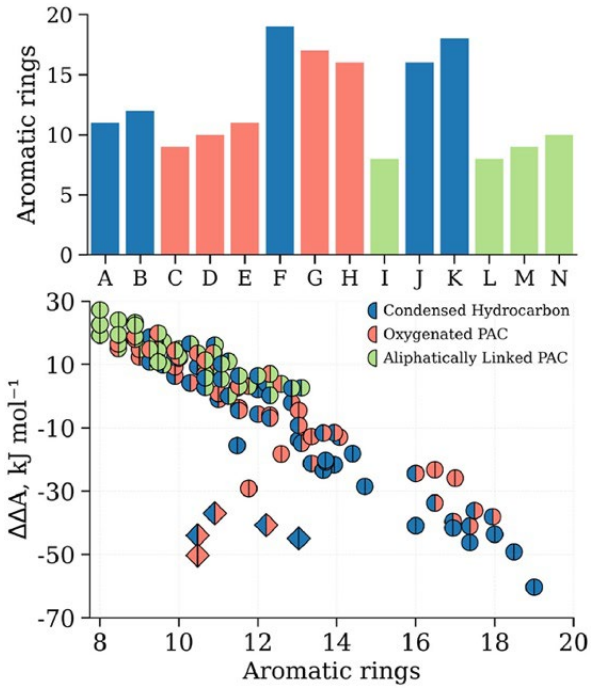

Figure 15. Relationship between the number of aromatic rings and dimerization FE. Top: Number of aromatic rings associated with each dimer. Bottom: Aggregation propensity compared to average number of aromatic rings in the dimer. PAC: polycyclic aromatic compound.

The success of such ML-based predictions in predicting free-energy barriers (ΔA) is shown in Figure 16. Moreover, Lasso regularization in the ML model helped us to extract critical features of importance by providing valuable insights regarding their influence on the dimerization ability of PAHs. Detailed discussions regarding these results were already provided in our previous annual efforts and hence are not repeated here for brevity.

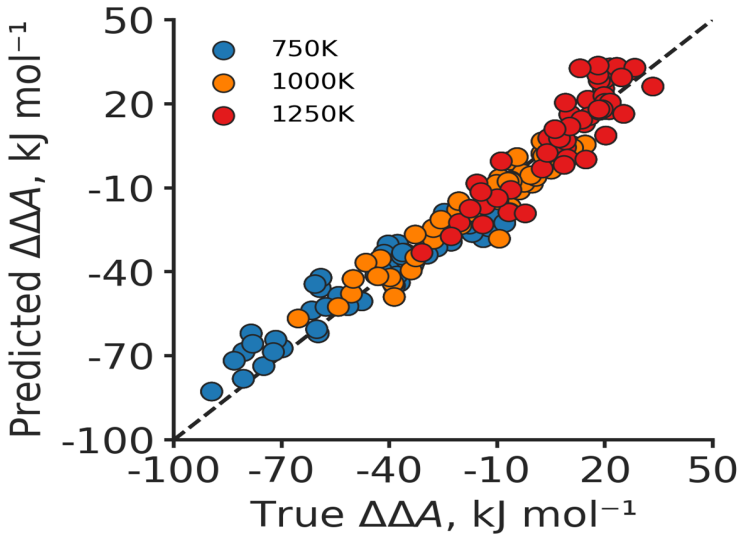

Figure 16. ML-assisted free-energy barrier analysis across a range of conditions.

In recent efforts, we closely collaborated with RTRC kinetics to identify PAH species available in the gas phase mechanism. A reduced nanoparticle inception model was then developed using our framework. The model used information on the PAH species benzopyrene (A_4R_5). The optimized rate constant can be approximated as shown in Equation 1.

$$k_f \left(\frac{L}{mol.s}\right) = \text{A T exp -} \left(\frac{G_f}{RT}\right) \quad \text{(Eq. 1)}$$

In this equation, the preexponential factor (A) is obtained as 2.0837×10^{10} 1/K/s, whereas the activation free energy is computed as

$$G_f \text{ (kJ/mol)} = g_o + g_1 T + g_2 T^2 \quad \text{(Eq. 2)}$$

g_o, g_1, and g_2 are the constants with respective uncertainty as noted below.

$$\begin{aligned} g_o &= \text{-4.12147} \quad \text{+/- 0.4233} \quad (10.27\%) \\ g_1 &= 0.101723 \quad \text{+/- 0.001069} \quad (1.051\%) \\ g_2 &= \text{5.55181e-06 +/- 5.515e-07} \quad (9.935\%) \end{aligned} \quad \text{(Eq. 3)}$$

Finally, this information is provided to the models described in Task 3 for MC simulations of post-inception growth as well as the nucleation rate expression in the moment-based soot model at GT.

Major Accomplishments

- Established a machine-learning-enabled MD framework, providing a reusable approach for future studies involving fuel-chemistry-dependent soot formation under relevant flame conditions.
- Developed a reduced nanoparticle inception model based on benzopyrene (A_4R_5) for coupling with both MC simulations and the moment-based soot model at GT for RQL combustor-relevant conditions.

Publications

Peer-Reviewed Journal Publications

Baranwal, M., Saldinger, J. C., Kim, D., Elvati, P., Hero, A. O., & Violi, A. (2024). SPIN: A data-driven model to reduce large chemical reaction networks. *Fuel*, *367*, 131299.

Di Liddo, L., Saldinger, J. C., Jadidi, M., Elvati, P., Violi, A., & Dworkin, S. B. (2022). Exploring soot inception rate with stochastic modelling and machine learning. *Combustion & Flame, 258,* 112375.

He, T., Kim, D., Dillstrom, T., Cai, K., Zhang, P., Liu, C., He, X., Wang, Z. & Violi, A. (2021). Oxidation of 2,6-dimethylheptane at low temperature: Kinetic modeling and experimental study. *Fuel*, 287, 119220.

Kim, D., & Violi, A. (2021). On the importance of species selection for the formulation of fuel surrogates. *Proceedings of the Combustion Institute, 38*(4), 5615-5624.

Kim, D., & Violi, A. (2022). Uncertainty-based weight determination for surrogate optimization. *Combustion and Flame, 237*, 111850.

Saldinger, J. C., Elvati, P., & Violi, A. (2021). Stochastic and network analysis of polycyclic aromatic growth in a coflow diffusion flame. *Physical Chemistry Chemical Physics, 23*(7), 4326-4333.

Saldinger, J.C., Elvati, P., & Violi, A. (2023). A machine learning framework to predict the aggregation of polycyclic aromatic compounds. *Proceedings of the Combustion Institute*, 39(1),1009-1017.

Saldinger, J. C., Elvati, P., Alrawi, K., & Violi, A. (2024). Predicting aggregation rates of polycyclic aromatics through machine learning. *Fuel*, *364*, 131031.

Shao, C., Wang, Q., Zhang, W., Bennett, A., Li, Y., Guo, J., Im, H. G., Roberts, W. L., Violi, A. & Sarathy, S. M. (2023). Elucidating the polycyclic aromatic hydrocarbons involved in soot inception. *Communications Chemistry*, *6*(1), 223.

Shi, X., Wang, Q., & Violi, A. (2021). Reaction pathways for the formation of five-membered rings onto polyaromatic hydrocarbon framework. *Fuel*, 283, 119023.

Wang, Q., Saldinger, J. C., Elvati, P., & Violi, A. (2021). Molecular structures in flames: A comparison between SNapS2 and recent AFM results. *Proceedings of the Combustion Institute, 38*(1), 1133-1141.

Outreach Efforts

None.

Awards
None.

Student Involvement
One PhD student, J. Saldinger, contributed to this work.

Plans for Next Period
None.

Task 3 – Surface Growth and Aggregation Modeling
Raytheon Technologies Research Center

Objective
The objective of this task is to develop a physics-based framework for the prediction of soot particle growth after the inception process. The growth consists of agglomeration due to collisions between the primary particles and surface growth as a result of direct deposition of the precursors on the aggregate. The final aggregate fractal structure and its temporal evolution as a function of local conditions are of interest. This model provides the morphology characteristics of soot aggregates.

Milestone(s)
- Formulate a one-way coupled methodology to study fractal growth of soot particles along the conditions inside the combustor.

Research Approach
Soot particles from nucleation stages undergo various surface growth processes and form primary particles. These primary particles are spherical in nature and typically formed in the diameter range of 1-10 nm. The studies conducted under this effort will bridge the gap between formation of primary particles and their transformation into fractal aggregates through processes of surface growth and aggregation. Experimentally it is witnessed that structures of these soot particles are dependent on the local conditions (e.g., φ). These surface growth processes can occur because of heterogenous reactions of gas-phase precursors on solid soot particle surfaces (reaction limited growth) or through transport of soot precursors in high-speed flames (transport limited growth). Majority of growth models only account for reaction limited growth, ignore transport limited growth as well as cluster-cluster interactions which are important in aggregate formation. In this work, information on background gas-phase species contributing to soot particles (Kinetics RTRC) and the structure of initial soot nuclei (MD studies from Michigan) and the local conditions (Pressure, Temperature, equivalence ratio, diffusion of precursors) is merged to understand the fundamental processes contributing to formation of large soot aggregates. The transport limited growth is modelled through phase-field formulation.

At first, a blended model for transition from reaction limited growth to transport limited growth is achieved. As shown in Figure 17, the current model can predict the transition from fractal shape to spherical morphology of soot particles with increasing equivalence ratio. Anisotropy of aggregates and their fractal dimensions are two important factors that determine the shape of soot aggregates formed. The sensitivity of these aggregates with background equivalence ratio and the primary particle number density after nucleation is studied.

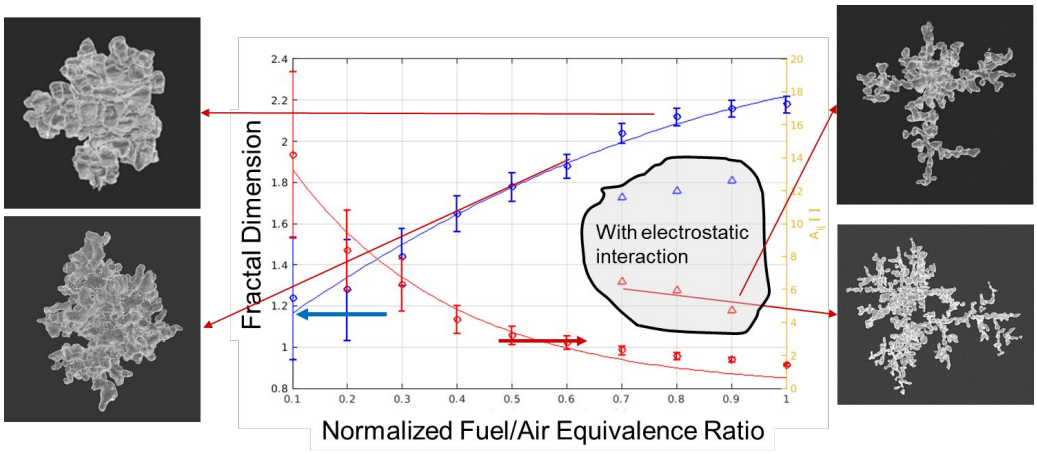

Figure 17. Phase field simulations to predict the aggregate structures.

The coupling between the growth framework being developed at RTRC with MD simulations from UM and the LES study at GT is briefly highlighted in Figure 18. The growth module takes the number density and size distribution of incipient soot particles from nucleation as an input and tracks the growth of such particles along the statistically averaged path lines, which have varying background LES conditions in form of temperature (*T*), pressure (*P*) and local equivalence ratio (ϕ), as detailed below. The output from such studies in the form of the parametrized fractal dimension (D_f) will be fed back into the LES-method of moment soot approach.

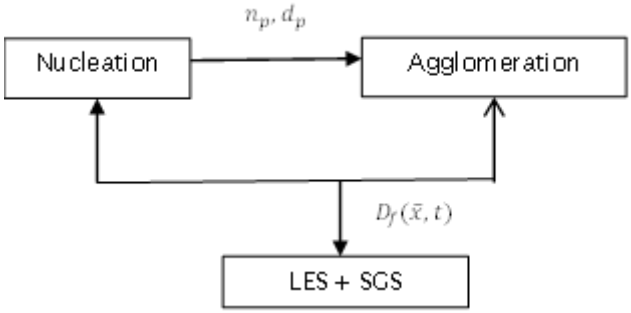

Figure 18. Post-inception growth of soot particles (LES-RTRC-UM coupling). LES: large eddy simulation, SGS: subgrid-scale.

The developed post-inception growth model described in previous annual effort has shown to capture the effect of different operating conditions on the growth characteristics of the particles, including size and morphology. The parametric exercise of this model, however, could become computationally prohibitive if one is to sweep over a range of operating parameters and combinations therein. A path line-sampling approach was proposed (schematic in Figure 19) where the full flow-field (obtained by the LES) is represented through statically sampled path lines over which the operating conditions would be time-variant. For example, the temperature and fuel/air ratio would evolve over the course of time as a particle moves from the injector towards the exit of the combustor. This time-history is then provided to the growth model where the variation of particle characteristics will be solved over the course of this timeframe for each individual path-line histogram (example output shown in Figure 20). This information can then be fed back into the LES with time-space mapping through the path line coordinates and nearest-point interpolation to provide full spatial representation of growth information which is then used in the moment soot approach. This approach effectively reduces the computational overhead of the growth model to a dozen simulations (assuming that this number of path lines is sufficient to properly sample the combustor flow field) compared to potentially hundreds in the conventional parametric approach. One should note that this is considered a one-way coupling approach where it is assumed that the macroscopic changes in the flow-

field due to the interaction with the soot-particle transport have negligible impact on the growth characteristics of the particles.

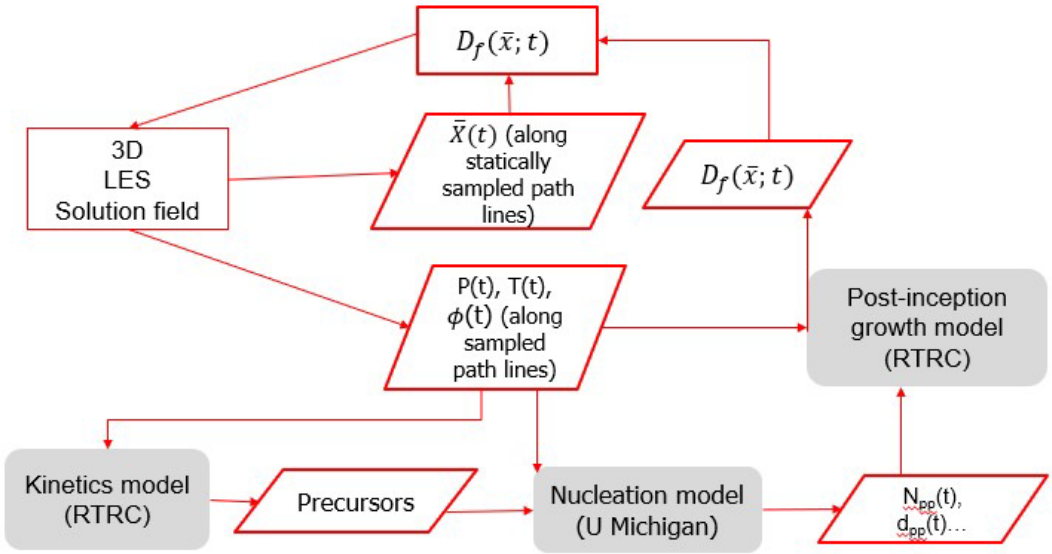

Figure 19. One way coupled strategy for growth of soot particles. LES: large eddy simulation, RTRC: Raytheon Technologies Research Center.

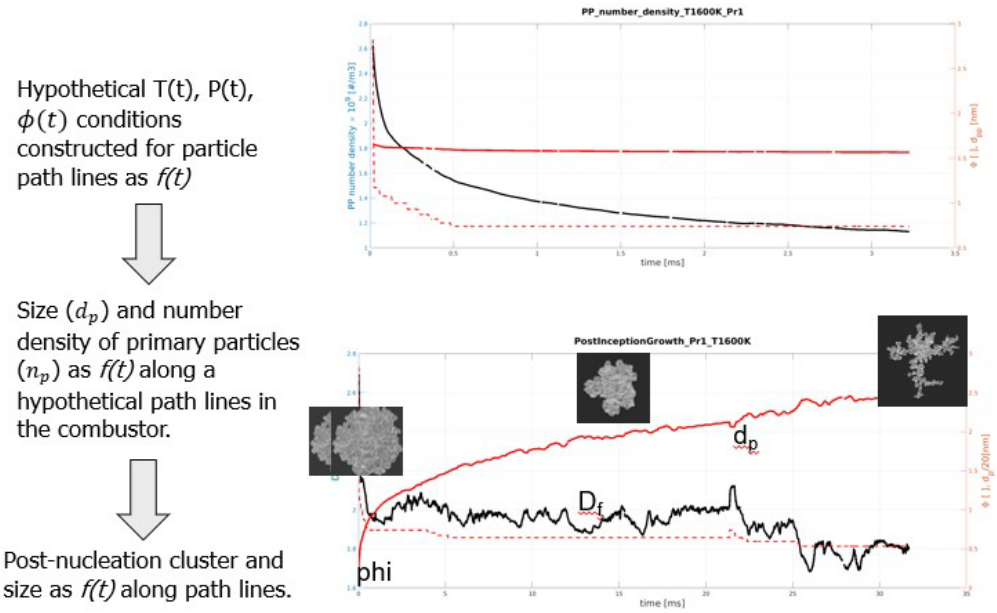

Figure 20. Demonstration of one-way coupled strategy along hypothetical large eddy simulation (LES) path-line.

To establish this methodology, the post inception growth modeling framework and the coupling therein to the LES framework is demonstrated for the solution of National Aeronautics and Space Administration (NASA)-LDI geometry for which LES solution was obtained from GT. The information along statistically sampled path lines is provided to the post-inception model which then solves the evolution of the soot clusters along those path lines. In order to get a sense of primary particle size and number density, a classical nucleation theory was used which takes the following form.

$$N_0(t) = [M(t)] \exp\left(-\frac{\Delta G_0(t)}{kT}\right) \quad \text{(Eq. 4)}$$

It is worth noting that this formulation or terms therein is eventually replaced by the solution of the molecular dynamics simulation. An example of primary particle number density along one of the path lines in the rig is shown in Figure 21. Figure 22 shows the evolution of soot particle characteristics (fractal dimension and average size) along two of the path lines inside the combustor.

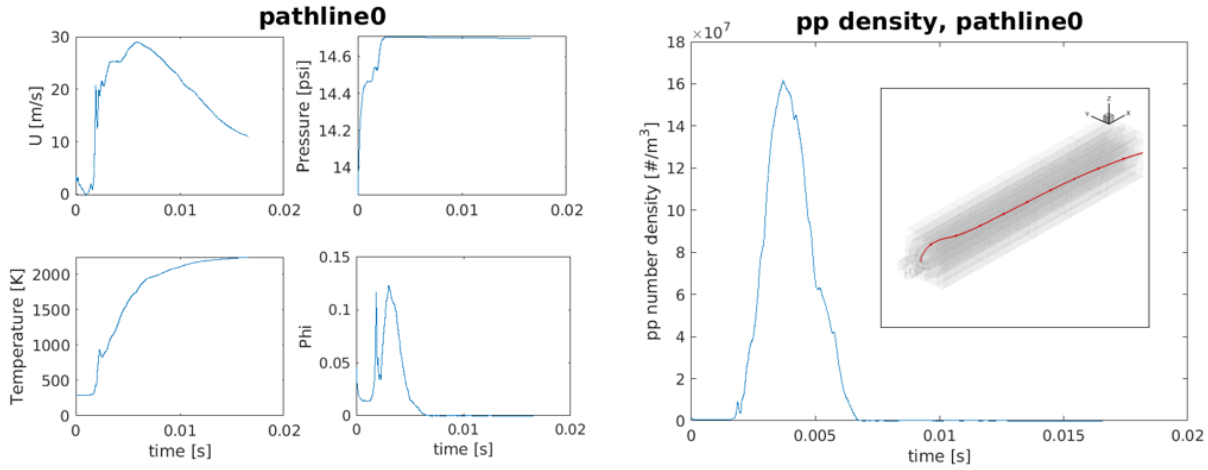

Figure 21. Variation of flow parameters along one path line in the combustor (left) and calculated primary particle number density using classical nucleation theory (right).

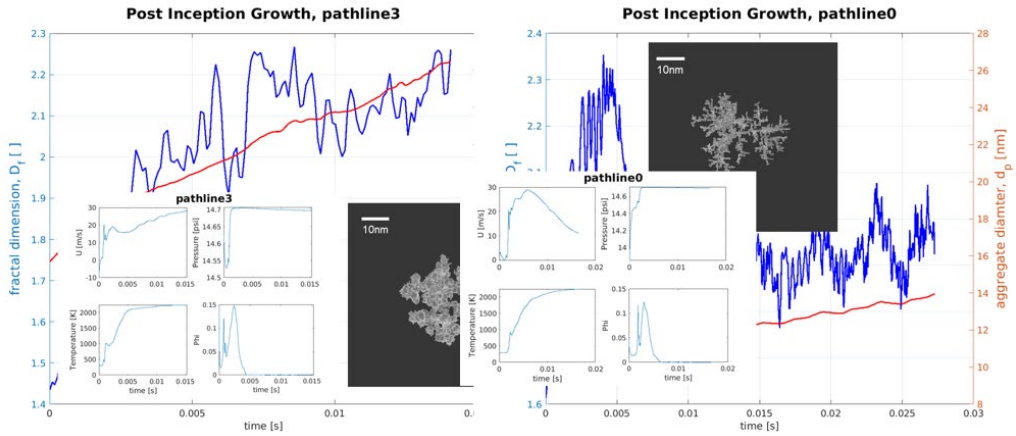

Figure 22. Evolution of soot particle characteristics along two path lines within the lean direct injection (LDI) combustor.

The demonstration along with the NASA LDI combustor provided confidence to use the framework for RQL combustor as highlighted in Figure 23.

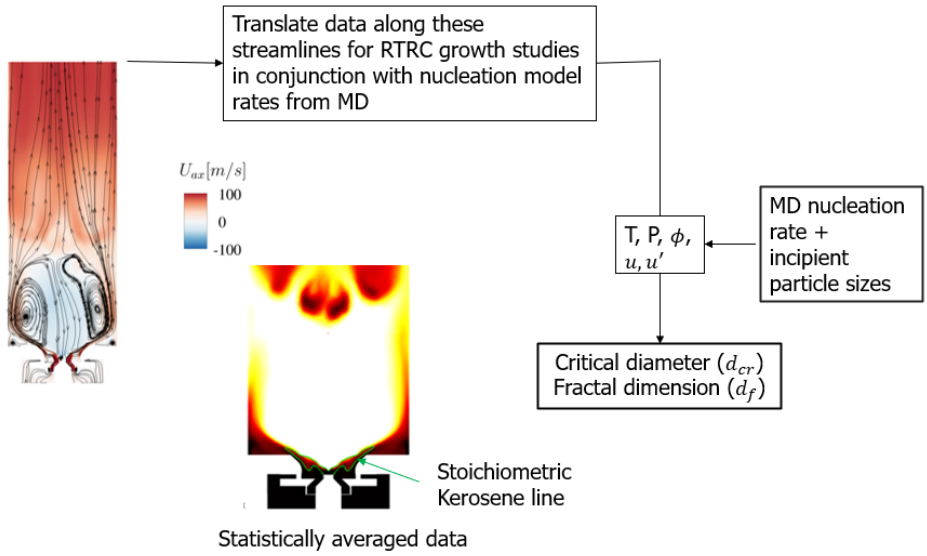

Figure 23. One-way coupled data along the rich-burn quick-mix lean-burn (RQL) computational fluid dynamics (CFD) Streamlines. MD: molecular dynamics, RTRC: Raytheon Technologies Research Center.

A parametric graph was generated to understand variation of fractal dimension (D_f) as a function of local mixture stoichiometry and the temperature conditions at different residence time available for soot particles to grow (see Figure 24). This coarse information was provided to GT in order to investigate its effects on the global soot output from moment models.

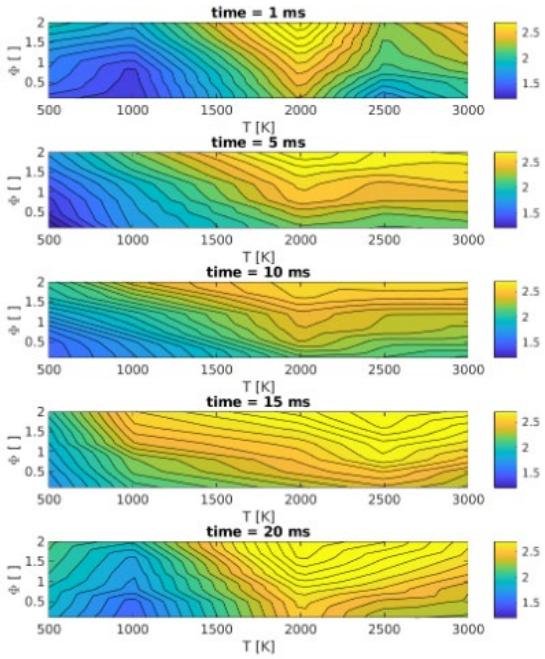

Figure 24. Fractal dimension as a function of parametric background conditions in rich-burn quick-mix lean-burn (RQL).

Major Accomplishments

Established one-way coupled methodology to study fractal growth of soot particles along the conditions inside the combustor.

Publications

None.

Task 4 – Large-Eddy Simulation

Georgia Institute of Technology

Objective

The objective of this task is to establish the soot modeling capabilities, use it within a physics-informed LES framework to model soot formation in turbulent reacting configurations, focusing on both canonical and complex settings, and eventually couple the inputs from Task 1-3 in the soot model to demonstrate the framework's ability and sensitivity to predict soot formation in a spray combustor of practical relevance.

Milestone(s)

- Develop and establish an LES–MOM methodology for sooting simulations of canonical and complex flames.
- Integrate components developed in Tasks 1–3 into the MOM soot framework and evaluate their relative impact against the baseline model.

Research Approach

LES studies of turbulent sooting problems are challenging because of the multiscale nature of soot inception, coagulation, and surface growth that must be modeled in a highly turbulent and reactive environment, typically in a complex combustor. Most prior studies have focused on global models that approximate small-scale physics. Consequently, many available models account for the underlying physics. In contrast, simulations require some approximations, because the computational resources will never meet the simulation requirements. In the current effort, we balance contributing to the

prediction of soot formation physics in a realistic gas turbine combustor with the need to obtain high-fidelity, reliable predictions by using advanced models. To achieve this goal, we leverage our past LES capability with baseline soot models. The original method of moments with interpolative closure (MOMIC) model (Frenklach, 2002) is also reapproximated to three-equation moment-based model (Nmira et al., 2023) to account for the key components of aggregate formation. The capabilities of implemented framework within LES are demonstrated in a range of canonical and complex sooting flames. Additionally, a multiscale LEM based strategy is established to upscale the small-scale soot processes towards the resolved LES scales and demonstrated in a 1D turbulent premixed flame simulation. However, coupling all these inputs in a fully resolved LES is computationally prohibitive especially in the final RQL spray sooting flame simulation, and hence a reduced order modeling approach based on reactor network modeling is utilized to compare the predictive capabilities of the model components assembled through Task 1- Task 3.

4.1 Modeling Framework

The full set of compressible reacting multispecies Navier–Stokes equations cannot be solved directly, because a direct numerical simulation is not feasible for practical applications. For LES, the large-scale flow features are resolved, and subgrid modeling is used for the smaller scales. The LES governing equations for a reacting sooting spray flame are obtained by filtering the compressible form of Navier-Stokes equations using a low-pass filter with a cut-off length equal to the grid size (Δ).

$$
\begin{aligned}
&\frac{\partial \bar{\rho}}{\partial t} + \frac{\partial}{\partial x_i}(\bar{\rho}\,\widetilde{u_\iota}) = \widetilde{\dot{\rho}_s} \\
&\frac{\partial}{\partial t}(\bar{\rho}\,\widetilde{u_\iota}) + \frac{\partial}{\partial x_j}\left(\bar{\rho}\,\widetilde{u_\iota}\,\widetilde{u_\jmath} + \bar{P}\,\delta_{ij} - \overline{\tau_{\iota\jmath}} + \tau_{ij}^{sgs}\right) = \widetilde{F_{s,\iota}} \\
&\qquad\qquad \frac{\partial}{\partial t}\left(\bar{\rho}\,\tilde{E}\right) + \frac{\partial}{\partial x_j}\left[\left(\bar{\rho}\,\tilde{E} + \bar{P}\right)\widetilde{u_\iota} + \overline{q_\iota} - \widetilde{u_\jmath}\,\overline{\tau_{\iota\jmath}} + H_i^{sgs} + \sigma_i^{sgs}\right] = \widetilde{\dot{Q}_s} + \widetilde{\dot{Q}_R} \\
&\frac{\partial}{\partial t}\left(\bar{\rho}\,\widetilde{Y_k}\right) + \frac{\partial}{\partial x_j}\left[\bar{\rho}\,\widetilde{Y_k}\,\widetilde{u_\jmath} - \bar{\rho}\,\overline{D_k}\,\frac{\partial \widetilde{Y_k}}{\partial x_j} + \Phi_{j,k}^{sgs} + \Theta_{jk}^{sgs}\right] = \bar{\rho}\,\widetilde{\dot{w}_k} + \widetilde{\dot{S}_{s,k}} \\
&\qquad \frac{\partial}{\partial t}\left(\bar{\rho}\,\widetilde{Y_{soot}}\right) + \frac{\partial}{\partial x_j}\left[\bar{\rho}\,\widetilde{Y_{soot}}\,\widetilde{u_\jmath} - \bar{\rho}\,\overline{D}_{soot}\,\frac{\partial\,\widetilde{Y}_{soot}}{\partial x_j} + \widetilde{V_T}_{soot}\,\widetilde{Y}_{soot} + \Phi_{j,k,soot}^{sgs} + \Theta_{jk,soot}^{sgs}\right] = \bar{\rho}\,\widetilde{\dot{w}}_{soot} \\
&\qquad\qquad \frac{\partial}{\partial t}\left(\bar{\rho}\,\widetilde{M_k}\right) + \frac{\partial}{\partial x_j}\left[\bar{\rho}\,\widetilde{M_k}\,\widetilde{u_\jmath} - \bar{\rho}\,\overline{D}_{soot}\,\frac{\partial\,\widetilde{M_k}}{\partial x_j} + \widetilde{V_T}\,\widetilde{M_k} + \Psi_{j,k}^{sgs} + \Omega_{j,k}^{sgs}\right] = \bar{\rho}\,\widetilde{\dot{M}_k} \\
&\frac{\partial}{\partial t}\left(\bar{\rho}k^{sgs}\right) + \frac{\partial}{\partial x_i}\left(\bar{\rho}\,\tilde{u}_i k^{sgs}\right) = -\tau_{ij}^{sgs}\frac{\partial\,\tilde{u}_i}{\partial x_j} - C_\epsilon\,\bar{\rho}\,\frac{k^{sgs\frac{3}{2}}}{\bar{\Delta}} + \frac{\partial}{\partial x_i}\left(\frac{\bar{\rho}\nu_T}{\mathrm{Pr}}\frac{\partial k^{sgs}}{\partial x_i}\right)
\end{aligned}
\qquad \text{(Eq. 5)}
$$

In the above equations, $\bar{\rho}$ is the filtered mass density, $\tilde{u}_i$ is the filtered velocity vector, $\bar{p}$ is the filtered pressure determined from the equation of state, $\overline{\tau_{ij}}$ is the filtered viscous stress, $\tilde{E}$ is the resolved energy per unit mass, $\bar{q}_i$ is the heat flux vector, $\tilde{Y}_k$, $\tilde{Y}_s$ are the gas-phase and soot mass fractions, and $\widetilde{M}_k$ is the filtered soot moment. The gas-phase governing equations contain source terms due to the Lagrangian dispersed phase ($\widetilde{\dot{\rho}_s}, \tilde{\dot{F}}_{s,i}, \widetilde{\dot{Q}_{s,\iota}}, \tilde{\dot{S}}_{s,k}$). Further information about the overall modeling can be found elsewhere (Panchal and Menon, 2022; Patel and Menon, 2008). $\widetilde{\dot{Q}_R} = \Sigma_\alpha 4\,\sigma\kappa_\alpha\left(\tilde{T}^4 - \widetilde{T_o}^4\right) + 4\,\sigma\kappa_{soot}\,\tilde{T}^4$ is the radiative heat loss term (Guo et al., 2004) in which κ_α is the Planck-mean absorption coefficient for gas-phase species $\alpha \in [CH_4, CO_2, H_2O, CO]$ and κ_{soot} is computed as $\kappa_{soot} = C_{soot}\,\tilde{f}_v\,\tilde{T}/4\sigma$, where C_{soot} is the soot radiation model constant assumed as 3.334 x 10^{-4} W/m3K5, f_v is the soot volume fraction. Contributions from subgrid radiation fluctuations in the radiative heat source terms are neglected presently. The terms $\widetilde{\dot{w}}_k$ represents the production rates of gas-phase species obtained using finite-rate chemistry approach which also includes the PAH species. The term $\widetilde{\dot{w}}_{soot}$ represents the production rate for soot consistent with the moment rate M1 (discussed later). The term D_{soot} associated with diffusion of soot is typically neglected. The thermophoretic term represented by $\tilde{V}_T$ is also neglected due to its overall lower contribution in turbulent flames.

The subgrid scale viscous stress tensor terms are modeled using local dynamic kinetic energy model (LDKM) (Menon & Kim, 1996). The subgrid enthalpy flux is modeled using eddy viscosity and a gradient assumption where turbulent Prandtl number (Pr_t) is assumed as unity. The subgrid diffusion of species is again also modeled using gradient-diffusion hypothesis with unity turbulent Schmidt number. A similar gradient-diffusion hypothesis ($\Phi_{j,k,soot}^{sgs}, \Psi_{j,k}^{sgs}$) is used for subgrid diffusion of soot scalar flux with a turbulent Schmidt number of 0.7. An additional challenge associated with turbulent combustion is the modeling of subgrid turbulence chemistry interaction terms unresolved on the LES grid. In the current

work, Partially stirred reactor based closure model is used in which the mixing time (τ_m) is calculated locally as $\tau_m = \sqrt{\tau_p \tau}_K$ where τ_p is the time scale of the largest eddy relevant for the mixing of the sub-grid and is computed as $\tau_p = \frac{\Delta}{\sqrt{2k_{sgs}/3}}$ and τ_K is the time scale relevant for the Kolmogorov length scale $\tau_K = \sqrt{\nu/\epsilon_{sgs}}$ where ϵ_{sgs} here represent the dissipation rate. Furthermore, the chemical time scale (τ_c) is computed using the laminar premixed flame thickness (δ_L) and flame speed (S_L) at stoichiometry. Once the relevant time scales are estimated, the filtered reaction source terms $\widetilde{\omega}_k$ are computed using filtered variables as $\widetilde{\omega}_k \approx \frac{\tau_m}{\tau_m+\tau_c}\, \dot{\omega}(\tilde{T}, \tilde{P}, \tilde{Y}_1.\tilde{Y}_2, \ldots., \tilde{Y}_k)$. This modeling approach has yielded satisfactory results in the past for referee rig simulations (Panchal & Menon, 2022) involving similar complexity to the current work. Modeling soot formation using LES presents additional difficulty associated with subfilter soot dynamics. In the current work, multiscale linear-eddy mixing based model is demonstrated to account for subgrid-turbulence-chemistry interactions in a 1D simulation. However, using this model within the subgrid of LES is computationally prohibitive especially for PAH-based MOM models and hence it is only demonstrated in a standalone manner. The subgrid effects are neglected for the present RQL simulations; however, they can be activated with enough computational resources. As the focus of the current work is soot modeling, the relevant formulation of baseline soot models is discussed. Figure 25 shows the key components of moment-based soot modeling.

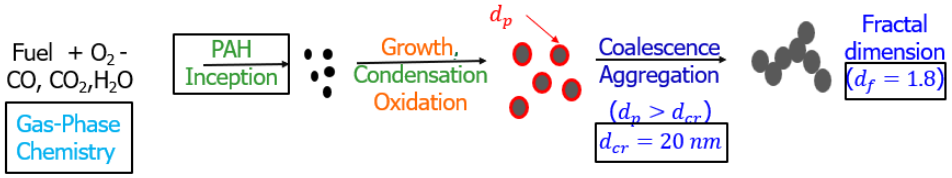

Figure 25. Key components of moment-based soot model. PAH: polyaromatic hydrocarbon.

The first component of the overall soot modeling is based on the gas-phase mechanisms that describe the oxidation of real fuel resulting in the formation of major product species such as CO_2 and H_2O along with key soot precursor species such as PAHs, C_2H_2, OH, etc. The baseline soot models employed in this work are based on MOMIC formulation (Frenklach, 2002). The MOMIC approach involves solving moment equations in two limiting conditions. In the coalescent limit where the soot particles are assumed to conserve the spherical shape after collision, the six moments are used where the equation of r-th moment M_r are solved in either the subgrid or in the resolved space along with the LES equations. A general form is $\frac{dM_r}{dt} = R_r + C_r + S_r + F_{M_r}$. r = 0,1,2,3,…,5 where M is the moment of the soot particle size distribution function (PSDF), and R, C, S, and F are respectively source terms due to nucleation, coagulation (in the coalescence limit), surface growth, and subgrid turbulent mixing contributions to the r-th moment equation. When soot particles exceed a certain size limit (dcr), the particles start to form chain-like aggregate structures of fractal dimensions (D_f = 1.8). The above equations are added with three other set of aggregate moments denoted by P_r with its own source terms, and their effects are included in the source terms of M_r i.e., aggregate rates, growth rates, coagulation rates in the non-coalescent limit resulting in total of nine moments. One key issue with these higher-order moments is that they can take very large or low exponents that can numerically explode. In such scenarios preserving the monotonicity of the original moments can become numerically cumbersome, especially important in logarithmic interpolative closures. Hence, in the present work, these nine moment formulations are converted to three moment formulation (Nmira et al., 2023), much easier to couple with CFD, where the particles are assumed to be monodisperse facilitating their numerical treatment in a more robust manner. This assumption has minor effects in comparison to other sources of chemical uncertainties on the overall predictions as discussed later. In this the zeroth moment, M_0, represents the number density (N_D) of the soot aggregates, the first moment (M_1) represents the soot mass concentration (Ycs), and the second moment represents the number density of the primary particle (N_{ps}). These moments are then later used to compute key global properties of engineering interests such as soot volume fraction ($f_v = M_1/\rho_s$), mean particle diameter $d_p = \left(\frac{6Y_{cs}}{\pi\rho_s N_{ps}}\right)^{1/3}$, mean number of primary particles per aggregate $n_p = \frac{N_{ps}}{N_D}$, and area density $A_s = \pi d_{ps}^2 N_{ps}$. The soot density ρ_s is assumed to be constant at 1,850 kg/m^3.

A brief description of kinetics models used to compute the corresponding source terms is provided here. Mainly two different soot kinetics models are available.

In the Lindstedt model (Leung et al., 1991), nucleation is assumed to occur via acetylene gas phase species. An empirical relation is used to correlate nucleation rate with acetylene concentration. A similar empirical relation is used to account for surface growth due to acetylene concentration. Oxidation is accounted for by the rate of expression involving O_2 oxidation. This kinetic model implemented within the MOMIC code and has been used within the subgrid LEM to simulate soot formation from turbulent premixed and non-premixed flames (El-Asrag et al., 2007; El-Asrag & Menon, 2009). A PM-ROM (discussed in Task 1) is an improvement in the rate coefficients of this model to better match with detailed PAH-based soot model (discussed next) and is also implemented in the modeling suite.

To account for detailed physics of soot formation processes rather than empirical relations involved in Lindstedt model, soot kinetic models that rely on PAH-inception and detailed growth pathways are also implemented. For three-dimensional (3D) LES, using detailed gas-phase kinetics with pathways for heavier PAHs till seven rings are not feasible computationally, and thus the reduced gas-phase mechanisms are considered which tracks growth of PAH formation only until naphthalene (A_2). However, higher PAH species such as pyrene (A_4), or benzopyrene (A_4R_5) can also be used in the same framework as long as they are part of reduced gas-phase chemistry. These PAH dimers are assumed to contribute to both nucleation and condensation processes. The PAH dimers resulting in nucleation are assumed to have a sticking efficiency γ_{PAH} and can be provided as an input to the code. Surface growth and oxidation reactions are assumed to occur using H-abstraction-C-addition mechanism. Soot particles are assumed to grow spherically until they reach a critical primary particle diameter (d_{cr}) of 10 nm beyond which they begin to form aggregates with a fractal dimension (D_f) of 1.8. Coagulation of soot particles is modeled across all three regimes free molecular, transitional, and continuum. Both the d_{cr} and D_f are provided as an input option to these models such that they can be changed following the aggregation characteristics obtained through MC studies in Task 3.

4.2 Verification and Sensitivity of Standalone Soot Models

Comparison of Zero-Dimensional (0D) PSR Simulation Framework

In these test cases, the soot models developed in the present work are evaluated using numerical simulations of 0D PSR configurations, for which reference data are available (Brown et al., 1998) using the MOMIC approach (see Figure 26). The operating conditions correspond to an ethylene–air premixed mixture at equivalence ratio ϕ = 2.5, temperatures ranging from 1,500–2,000K, and a reactor residence time of 8.5 ms. Three different soot kinetics models are investigated: (1) the MOMIC approach with Leung and Lindstedt (LL) soot kinetics (Leung et al., 1991), (2) the MOMIC model with PAH-based soot kinetics, and (3) a monodisperse (MONO) formulation of MOMIC. A detailed 99-species Wang–Frenklach ethylene–air mechanism (Wang & Frenklach, 1997) is employed to account for PAH formation pathways up to pyrene, and soot inception is assumed to occur via pyrene dimerization.

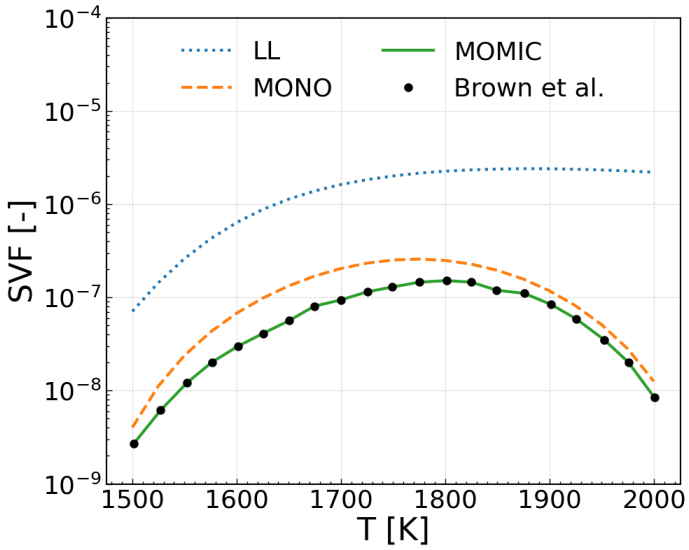

Figure 26. Comparison of the present soot models with zero-dimensional (0D) perfectly stirred reactor (PSR) simulations (Brown et al., 1998). LL: Leung and Lindstedt, MONO: monodisperse, MOMIC: method of moments with interpolative closure.

The LL-based MOMIC model fails to capture the characteristic bell-shaped dependence of soot volume fraction on temperature within the studied range, and it overpredicts soot levels by approximately an order of magnitude compared to the baseline MOMIC–PAH model. The reformulated monodisperse model closely matches the baseline MOMIC results, with only minimal deviations arising from the assumption of Monodispersity, whereas the MOMIC model successfully reproduces the reported data.

Sensitivity of Soot Modeling Components Using International Sooting Flame Workshop Data

As noted earlier in Figure 25, soot modeling is highly sensitive to several key components, including the underlying gas-phase chemistry, nucleation pathways, and post-inception aggregation processes. In this section, burner-stabilized laminar premixed ethylene–air flames at $\phi = 2.33$ are used to assess the sensitivity of the soot model to these components. Experimental data are obtained from the International Sooting Flame Workshop (Menon et al., 2007). The experimentally measured temperature profiles are directly imposed in Cantera[1] during simulations; thus, radiative heat-loss modeling is not required. For these assessments, the monodisperse version of the soot model is employed, and only one modeling component is varied at a time to systematically isolate its effect. To reiterate, the baseline soot model uses a three-moment formulation with pyrene-based nucleation, hydrogen-abstraction-C_2H_2-addition (HACA)-based surface growth and oxidation, and coalescent coagulation followed by aggregate formation once the primary particle diameter exceeds a critical value of 27.5 nm.

First, the influence of gas-phase chemistry is examined using four well-established kinetic mechanisms from literature. While the soot predictions obtained using the Slavinskaya mechanism (Slavinskaya & Frank, 2009) appear encouraging, the intent here is not to evaluate the absolute accuracy of each mechanism, but to quantify the relative variation in soot levels arising from changes in gas-phase chemistry. These variations strongly affect the predicted pyrene concentrations—the assumed soot precursor in this model (also emphasized in Task 1)—and lead to order-of-magnitude differences in soot volume fraction, as shown in Figure 27a.

The effect of nucleation modeling is evaluated while keeping the gas-phase mechanism Caltech mechanism [also inferred as robust mechanism in RTRC Task 1 activities] and other soot sub-models fixed. The simplest nucleation approach uses

[1] Cantera is an open-source suite of tools for problems involving chemical kinetics, thermodynamics, and transport processes. Cantera is a sponsored project of NumFOCUS®, a 501(c) nonprofit charity in the United States. NumFOCUS is a registered trademark of NumFOCUS, Inc., Austin, Texas.

the semi-empirical acetylene-based expression of Leung and Lindstedt, whereas the PAH-based formulations assume inception via naphthalene and pyrene pathways (with the capability to include heavier PAHs up to A7, discussed in Task 2, when supported by the gas-phase mechanism). For the pyrene-based models, the dimerization efficiency (γ_{A_4}) is also varied. As shown in Figure 27b, the choice of nucleation pathway and dimerization efficiency has an impact comparable in magnitude to the gas-phase mechanism variations, underscoring the need for accurate representations of PAH concentrations and their dimerization chemistry.

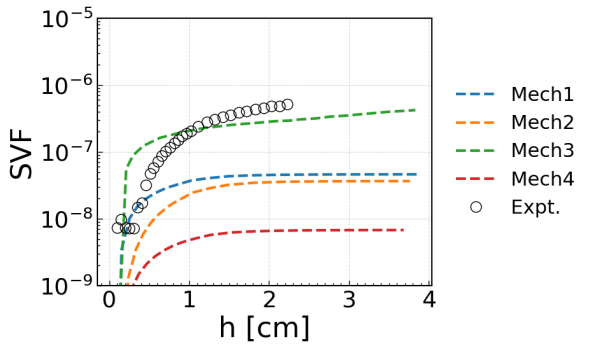

(a) Effects of gas-phase mechanism
Mech 1: ABF, 2001
Mech 2: CalTech, 2009
Mech 3: Slavinskaya, 2009
Mech 4: WF, 1999

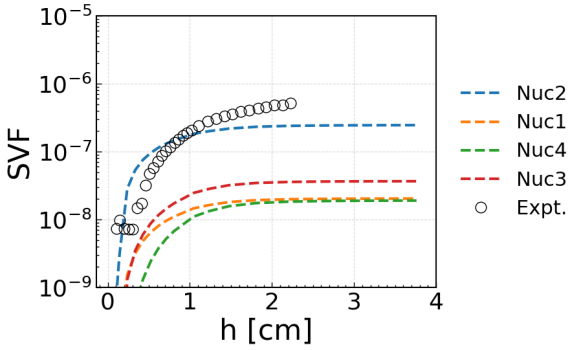

(b) Effects of nucleation mechanism
Nuc 1: C_2H_2-based
Nuc 2: Naphthalene-based ($\gamma_{A_2} = 1.0$)
Nuc 3: Naphthalene-based ($\gamma_{A_4} = 1.0$)
Nuc 4: Pyrene-based ($\gamma_4 = 0.025$)

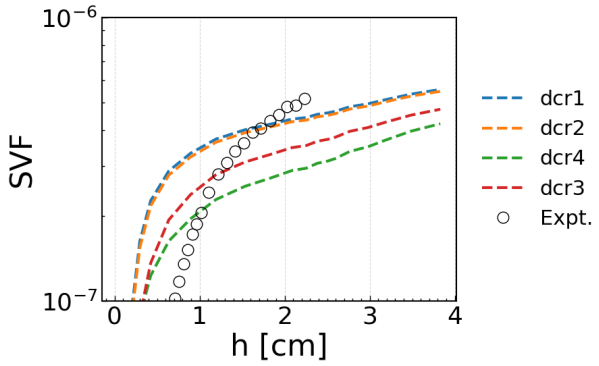

(c) Effects of variation in transition from coalescence to aggregation
dcr1 : 1 nm, **dcr2** : 5 nm, **dcr3** : 10 nm, **dcr4** : 27.5 nm

Figure 27. Illustrations of sensitivities of soot predictions to gas-phase kinetics, nucleation models, and the aggregation parameters using Internation Sooting Flame-target Bunsen burner stabilized laminar premixed flame.

Finally, the effect of varying the aggregation transition criterion (d_{cr}) is examined. Decreasing d_{cr} leads to earlier formation of aggregate structures, which increases the effective surface area available for surface reactions, resulting in higher soot volume fractions. However, these effects are smaller relative to the variations caused by gas-phase kinetics and nucleation modeling. Although surface growth contributes significantly to soot mass addition, the corresponding HACA kinetics are not varied here due to broad agreement in the literature, with remaining uncertainties discussed later.

Overall, these analyses highlight the strong sensitivity of soot formation to the selected gas-phase mechanism, nucleation chemistry, and aggregation physics. The soot modeling framework developed in this project is modular, allowing new or modified sub-models to be incorporated easily. This soot modeling suite is subsequently integrated into the in-house compressible LES solver LESLIE.

4.3 Modeling Canonical Soot Formation with LESLIE

The verified standalone soot modeling frameworks are coupled with the in-house compressible flow solver LESLIE and then used to investigate soot formation in a range of canonical flame configurations. As the accurate description of PAH species requires detailed mechanism of O(100) species, making their direct integration in 3D LES is computationally prohibitive. To mitigate these challenges, often tabulated strategies have been preferred in literature. Although such approach is computationally efficient, their assumptions of equilibrium chemistry and nature of tabulation remain questionable in spray flames due to partial premixing, product-reactant mixing, and the interactions of wide spatial and temporal scales of soot with turbulence. Finite-rate-chemistry LES, on the other hand, can account for such shortcomings; however, they become computationally intractable, especially for sooting simulations where details of PAHs have to be included. Therefore, to make these simulations feasible, few approximations are necessary. Specifically, to conduct these simulations, reduced gas-phase mechanisms are used that track the growth of PAH species till naphthalene.

Verification in Laminar Premixed Flames

The implemented soot modeling framework, integrated with reduced gas-phase chemistry (Bisetti et al., 2012), is verified against experimental data for a canonical premixed ethylene–air flame. A rich laminar premixed flame (Menon et al., 2007) at $\phi = 2.64$ is simulated under two conditions: (1) with radiation modeling and (2) without radiation modeling. As shown in Figure 28b, numerically predicted soot volume fractions exhibit reasonable agreement with experimental measurements. Furthermore, the complex dependence of soot formation on temperature (see Figure 28a) is evident: when radiation is included, at lower temperatures, soot levels are lower, suggesting consistency with lower temperatures of soot-bell curve.

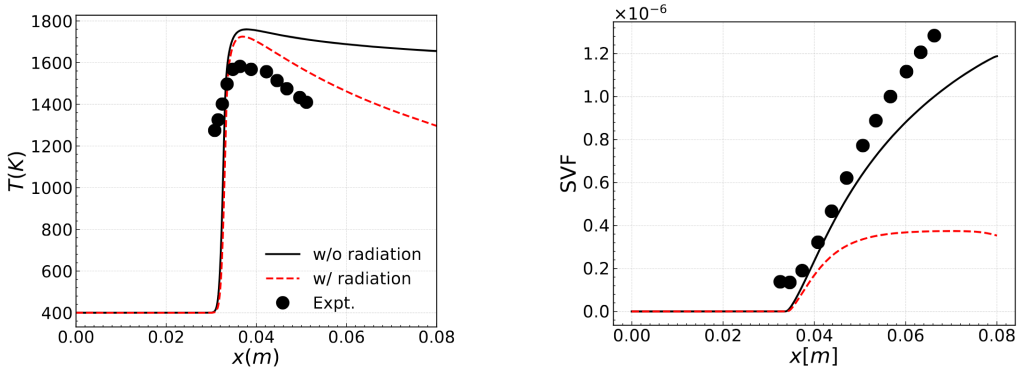

Figure 28. Comprison of (a) temperature and (b) soot volume fraction predictions in lamiar premixed ethylene-air flames with and without radiation. Expt. represents experimental data by Menon et al., 2007.

2D Mixing Layers from Jet-A Fuel

In this section, 2D calculations of temporal mixing layer with gasified Jet-A fuel are performed. A representative 2D strip (width H = 15 mm) of Jet-A fuel (diluted with 85 % N_2 by volume) is surrounded with air (21 % O_2 and 79 % N_2 in volume), as shown in Figure 29. The rectangular computational domain is around 94 mm long in a direction parallel (horizontal) to the fuel strip and 105 mm wide in a direction perpendicular to the fuel strip. Both the oxidizer and the fuel strip are atmospheric pressure. The air stream is preheated to 800K to increase resistance of the flame to extinction induced by the strain. The computational domain is discretized in a uniform mesh with total 1,048,576 cells (1,024x1,024), which corresponds to the minimum grid spacing of $\Delta x = \Delta y = 91.5$ micron. This resolution is equivalent to the resolutions of direct numerical simulations (DNS) studies. Characteristic non-reflecting outflow boundary conditions are imposed in a direction perpendicular to the fuel strip (vertical) and periodic boundary conditions are applied in the other direction. The fuel strip moves to the right at a velocity of 8.74 m/s while the air co-flow moves in the opposite direction with the same

speed. For initialization, the temperature and species mass fractions are taken from a flamelet and mapped from mixture fraction space onto the crosswise direction using a mixture fraction profile.

$$z(y) = \frac{1}{2}\left[\mathrm{erf}\left(\frac{\frac{1}{2}\delta+y}{\sqrt{2\sigma_1^2}}\right) + \mathrm{erf}\left(\frac{\frac{1}{2}\delta-y}{\sqrt{2\sigma_1^2}}\right)\right] \quad \text{(Eq. 6)}$$

Here, y represents the spatial location in a perpendicular direction, the parameter δ controls the width of fuel strip and the slope parameter σ_1 controls the slope of the profile. The values of these parameters were taken as 7.5 mm and 1.8. The simulations are conducted using the 62 species reduced chemical kinetics model for Jet-A fuel developed under NJFCP.

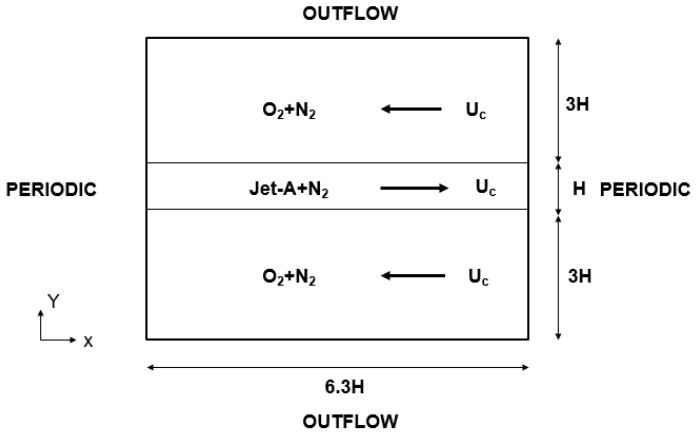

Figure 29. Schematic of temporal mixing layer of Jet-A fuel.

Figure 30 shows the contours of evolution of soot number density overlapping with isolines of temperature. The mixing layer grows with time, and the simulations are continued till time reaches 20 ms, when large structure forms. As can be seen, the growth of shear layers causes the wrinkling of the flame. The soot number density follows closely with the pyrene formation zones in the non-premixed flames as the nucleation process is assumed to occur through pyrene dimerization. Figure 31 shows the average profiles of u velocity normalized with $U_{o,}$ number density of soot particles formed and soot mass fractions profiles. The quantitative magnitudes of soot mass fraction (~10^{-4}) as well as the number density (~10^{12} 1/cm^3) match well with the values reported in Atilli et al. (2014), whereas the soot models in their studies were different than the one used in the present work.

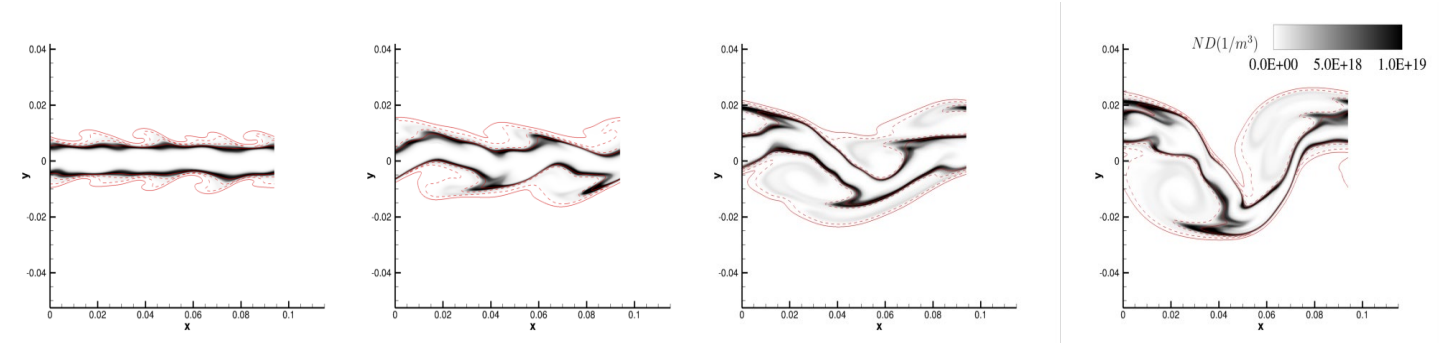

Figure 30. Contours of soot evolution overlayed with isolines of temperature T=1600K (----) and T=2000K (—).

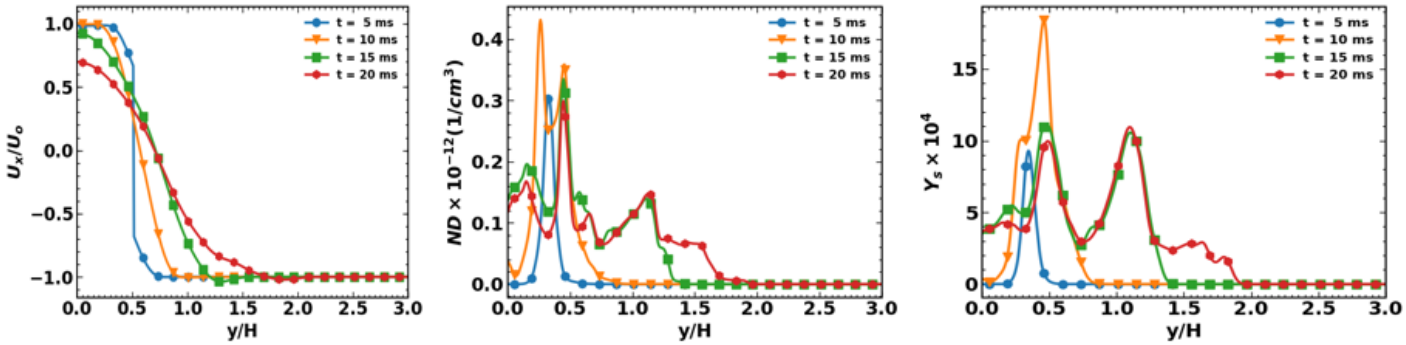

Figure 31. Spatially averaged profiles of velocity, soot number density and soot mass fractions.

3D LES of Gas-Phase Turbulent Premixed Flame Propagation (TPF)

We performed 3D calculations of turbulent premixed flames of gasified Jet-A2 fuel as a final investigation case. The schematic for the configuration is shown in Figure 32. Specifically, the laminar premixed flames investigated in the earlier section are superimposed on top of the isotropic turbulence field such that the flame turbulence interactions fall in a thin reaction zone $\left(\frac{u'}{S_l} = 10 \,\&\, \frac{l}{\delta_f} = 6.2\right)$ where, u' represents the turbulence intensity, S_l represents the laminar flame speed, l represents the turbulent length scale and δ_f is the flame thickness. The grid resolution is 96x96x96 for a physical domain of 15x15x15 mm. Characteristic inflow-outflow conditions are applied in the streamwise direction whereas periodicity is applied in the cross-streamwise and spanwise direction. The initial turbulence field is generated using a well-developed DNS simulation of isotopic turbulence in the same periodic domain and then filtered back to the LES grid. Fuel kinetics is based on the same 41-species skeletal mechanism developed by T. Lu and coworkers at the University of Connecticut. To model the unresolved subgrid stresses, we employ a well-established LDKM. Additionally, we use the partially stirred reactor (PaSR) model to incorporate the effects of turbulence-chemistry interactions due to unresolved subgrid interactions between chemistry and turbulence. All the simulations are conducted using Georgia Tech's super-computing cluster (PACE-phoenix) with Intel® Ivy-bridge i7 processors.

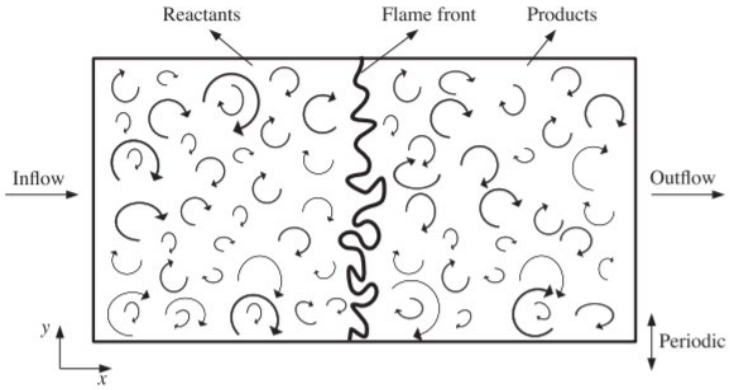

Figure 32. Schematic of the turbulent premixed flame.

Figure 33 shows the inflow and outflow vorticity contours as well as the wrinkling of the initially planar surface due to background turbulence. The overall qualitative zones of soot nucleation, growth, and oxidation behind the flame are shown in Figure 34. Moreover, as highlighted by the maximum contour lines of nucleation, surface growth, and oxidation

® Intel is a registered trademark of Intel Corporation, Santa Clara, California.

processes, the processes occur very close to each other in a thin zone; however, their relative magnitudes may differ significantly.

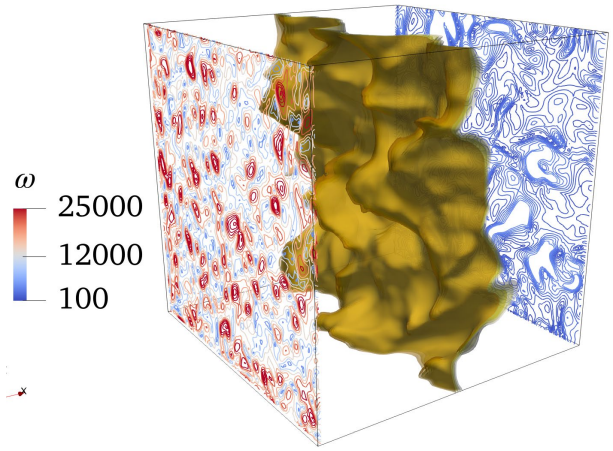

Figure 33. Vorticity magnitude (s^{-1}) at the inflow and outflow planes along with wrinkled flame surface.

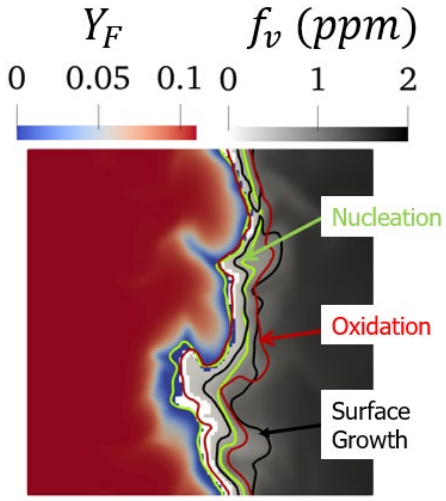

Figure 34. Consumption of gas phase fuel (left) formed soot levels (right) superimposed with contour lines of soot sub-processes in a turbulent premixed flame.

4.4 Upscaling the Soot Sources Using the Linear Eddy Mixing (LEM) Strategy

As shown schematically in Figure 35, the soot scalar fields in the above formulation are transported on the LES grid (LES-MOM). The central challenge, however, lies in accurately determining the soot source terms in an LES context. These sub-processes occur at subgrid scales, and the baseline source-term expressions are derived under quasi-steady assumptions, which are not directly valid in turbulent flows with strong spatial and temporal fluctuations. Therefore, the objective of this work is to develop a methodology, guided by high-fidelity, first-principles studies, to account for the multiscale evolution of soot source terms in turbulent environments. This provides a physically justified basis for incorporating soot models within LES frameworks.

$$< \frac{dM_i}{dt} > = \frac{d\widetilde{M}_i}{dt} + (SGS)_{model}$$

- LES – MOM: $< \frac{dM_i}{dt} > = f(\widetilde{M}_i, \tilde{T}, \tilde{Y}_i)$
  - Traditional LES/RANS-MOM methods models soot physics at "large" scales

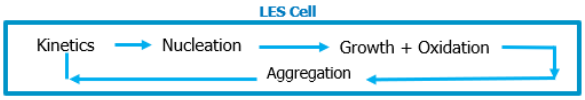

- Multiscale LES-(LEM+MOM) :
  - Does stochastic sub-grid model simulation within each LES cell

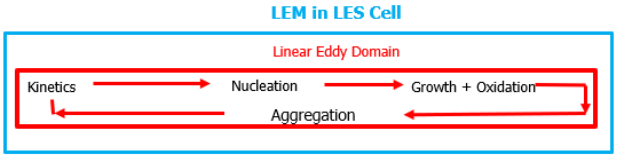

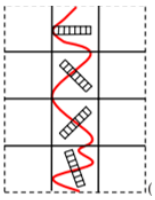

LEM Domain within LES Cells

Figure 35. Mixing based sub-filter soot scales. LEM: Linear Eddy Mixing, LES: large eddy simulation, MOM: method of moment, RANS: Reynolds-averaged Navier–Stokes.

To address this, we employed a standalone 1D LEM model (Srinivasan & Menon, 2014). Previous studies have used the combined LES+LEM–MOM approach (El Asrag et al., 2007) with a reduced 19-species gas-phase mechanism, which limits soot kinetics to simplified Lindstedt-type formulations. However, detailed PAH chemistry involves approximately 60 species and is inherently stiff; thus, in this work, the focus is placed on standalone LEM+MOM simulations to examine subgrid-scale turbulent mixing effects in premixed jet flames at two rich equivalence ratios and across different turbulence Reynolds numbers. The 1D nature of the LEM framework enables the use of a more detailed reduced jet-fuel mechanism, allowing PAH growth to be tracked up to pyrene. In this study, a 62-species reduced mechanism is employed, permitting nucleation modeling based on pyrene dimerization.

The standalone LEM model which has been used to simulate high Karlovitz number non-sooting turbulent flames in the past (Sreenivasan & Menon, 2014). It solves temperature evolution and species evolution through reaction-diffusion equations and is now coupled with additional soot moment scalars as represented mathematically below:

$$\begin{aligned}
\frac{\partial Y_k}{\partial t} &= F_{k,stir} - \frac{1}{\rho}\frac{\partial}{\partial s}(\rho Y_k V_k) + \frac{\dot{\omega_k} W_k}{\rho} \quad k = 1, \dots, N_g \\
\frac{\partial T}{\partial t} &= F_{T,stir} - \frac{1}{\bar{c_p}} \Sigma_{k=1}^{N} c_{p,k} Y_k V_k \frac{\partial T}{\partial s} + \frac{1}{\rho\,\bar{c_p}} \frac{\partial}{\partial s}\left(\bar{\kappa}\frac{\partial T}{\partial s}\right) - \frac{1}{\rho\,\bar{c_p}} \Sigma_{k=1}^{N} (h_k\, \dot{\omega}_k\, W_k) \\
\frac{\partial M_r}{\partial t} &= F_{M_r,stir} + \dot{\omega}_{M_r} \quad r = 0,1,2,3,4,5
\end{aligned} \qquad \text{(Eq. 7)}$$

Here ρ represents the two phase density, N_g denote the total number of gas phase species, $F_{k,stir}$ is the term for stirring for species mass fraction, M_r represents the soot moments, $F_{M_r,stirr}$ is the stirring for moment terms, $Y_k, h_k, \dot{\omega}_k, \dot{\omega}_{M_r}$ represent the mass fraction, enthalpy, reaction rate of the k_{th} species and r_{th} moment, $W_k, c_{p,k}, V_k$ denote the k_{th} species molecular weight, specific heat at constant pressure and diffusion velocity.

The turbulent effects are modelled using the triplet mapping procedure which rearranges the scalar field by the motion of an eddy. This approach has shown to reproduce the turbulent diffusion associated with high Re inertial range turbulence. The evolution of the scalar field within the LEM domain is shown in Figure 36.

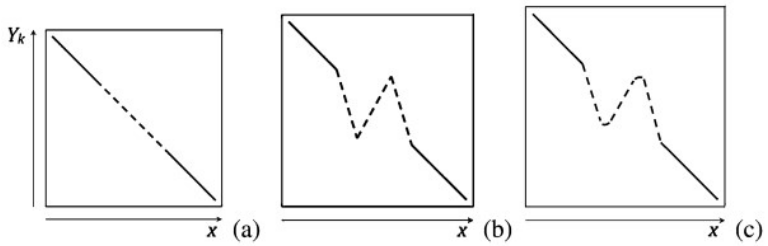

(a) Initial Scalar Field (b) After Triplet Mapping (c) after reaction-diffusion

Figure 36. Evolution of scalar field within linear eddy mixing (LEM) domain.

In this, the eddy size (l) is chosen from a turbulent PDF $f(l)$

$$f(l) = \frac{\frac{5}{3}l^{-\frac{8}{3}}}{\left(\eta_e^{-\frac{5}{3}} - l_o^{-\frac{5}{3}}\right)} \quad where\ \eta_e = N_n l_o Re^{-\frac{3}{4}} \qquad \text{(Eq. 8)}$$

The frequency of the stirring operations is estimated as

$$\lambda = \frac{54}{5}\left(\frac{\nu Re}{c_\lambda l_o^3}\right)\left[\frac{\left(\left(\frac{l_0}{\eta}\right)^{\frac{5}{3}} - 1\right)}{1 - \left(\frac{\eta_e}{l_0}\right)^{\frac{4}{3}}}\right] \qquad \text{(Eq. 9)}$$

Where η_e is the kolmogorv length scale, l_o is the integral length scale, Re_t is the turbulent Reynolds number and c_λ, N_n are the model constants. Based on the above two parameters, the eddy location is randomly selected from the permissible locations in the domain. The length of the 1D LEM domain is 25 mm, and the smallest grid size is 1μm. The laminar flame properties such as flame thickness ($\boldsymbol{\delta^o_{L,max}} = \frac{\nu}{S_l^o}$) and flame speed ($\boldsymbol{S_l^o}$) are provided in Table 1.

Table 1. Laminar flame properties of Jet-A fuel.

$\boldsymbol{\phi}$	$\boldsymbol{S_L^o}$ (m/s)	$\boldsymbol{\delta^o_{L,max}}$ (mm)	$\boldsymbol{\delta_T^0}$ (mm)
1.8	0.227	0.179	0.957
2.0	0.164	0.243	1.18

The turbulent cases simulated using LEM-MOM are given in Table 2. l_o represents the integral length scale, u' denotes the turbulence intensity; turbulent Reynolds number is defined as $Re_t = \frac{u' l_o}{\nu}$, Kolmogorov length scale is estimated as $\eta \sim l_o Re_t^{-3/4}$and Karlovitz Number is calculated as $Ka = \sqrt{\frac{\left(\frac{u'}{S_l^o}\right)^3 \delta_L^o}{l_o}}$. Since LEM-MOMIC is a stochastic model, the statistical averages over the 10,000 instantaneous snapshots are taken to obtain averaged flame profiles.

Table 2. Simulation parameters at different turbulent conditions.

Case	$\boldsymbol{\phi}$	$\boldsymbol{u'/S_L}$	$\boldsymbol{Re_t}$	$\boldsymbol{l_o}$ (mm)	$\boldsymbol{\eta}$ ($\boldsymbol{\mu}$m)	Ka
1A	1.8	10	83	2.0	72.8	9.46
1B	1.8	25	200	2.0	36.3	38.36
2A	2.0	10	83	1.9	91.1	11.02
2B	2.0	25	200	1.9	45.4	43.57

Figure 37 shows how the structure of flame changes because of isotropic 1D model turbulence by tracking the profiles of temperature. The thickening of flame with increasing Karlovitz number (Ka) is observed.

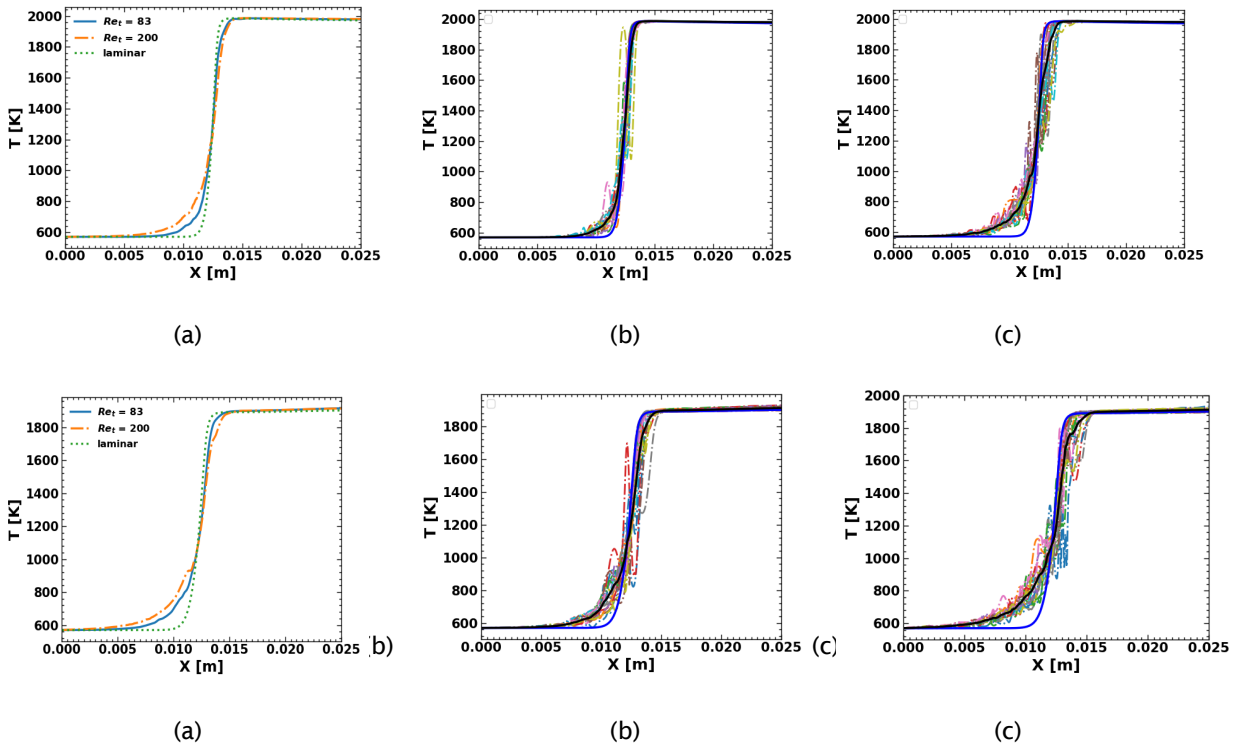

Figure 37. (a) Averaged profiles of temperature at laminar conditions, Re_t = 83 and Re_t= 200, (b) Representative instantaneous snapshots of temperature demonstrating action of eddies at Re_t = 83, and (c) Representative instantaneous snapshots of temperature demonstrating action of eddies at Re_t = 200. The top three figures present results for ϕ=1.8 while the bottom three figures show results for ϕ=2.0.

The main idea behind the current work is to understand the effects of turbulence due to different equivalence ratios as well as different turbulent conditions. The following Figure 38 shows how spatial variations of soot volume fraction and number density profiles occur. As expected, the rich flame shows more sooting behavior. For example, at $\phi = 2.0$ soot volume fraction levels are roughly four times more than that at $\phi = 1.8$. A similar effect is also observed on the soot number density profiles. The turbulence also seems to have a profound effect on the emissions levels. With increasing levels of turbulence, the levels as well as the initiation of soot formation seem to be affected. For example, at $\phi = 1.8$ the maximum soot volume fraction rises from 0.015 ppm to 0.025 ppm. Similarly, the initiation of soot inception also occurs earlier with increasing turbulence. The temperature profile suggests that the preheat zone thickens with increasing Re_t, and hence the pyrene formation as well as the soot inception due to pyrene (A_4) occurs earlier. To understand the physics of soot formation due to MOMIC model, we looked at the various source terms due to nucleation, coagulation and surface growth normalized with their maximum values to identify their locations of dominance behind the flame. A comparison of their locations is provided in Figure 39. The plot shows the competition between the nucleation, coagulation, and surface growth zones behind the flame in laminar and turbulent conditions. All these profiles are statistically averaged for stochastic comparison. The coagulation zone (CG) closely follows the nucleation (Nuc) zone. The combined effect of surface growth and oxidation is more dominant post nucleation.

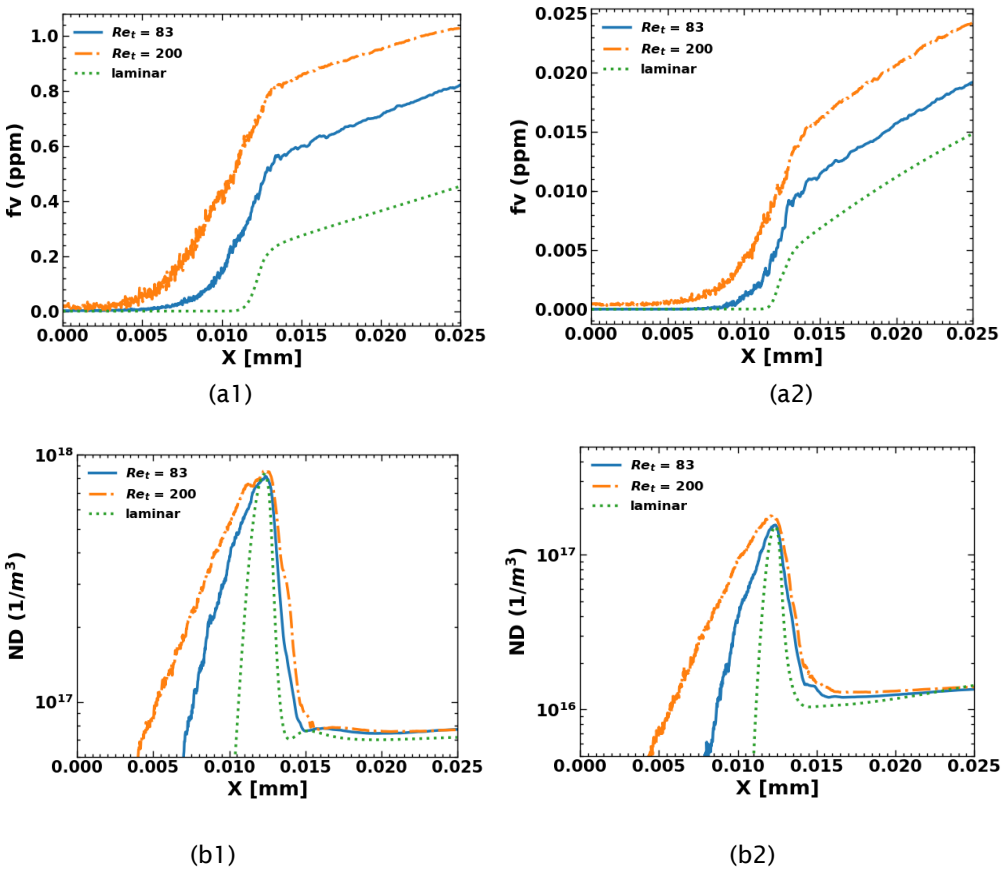

Figure 38. Comparison of soot volume fraction at laminar and turbulent conditions (a1) and (a2). Comparison of soot number density at laminar and turbulent conditions (b1) and (b2).

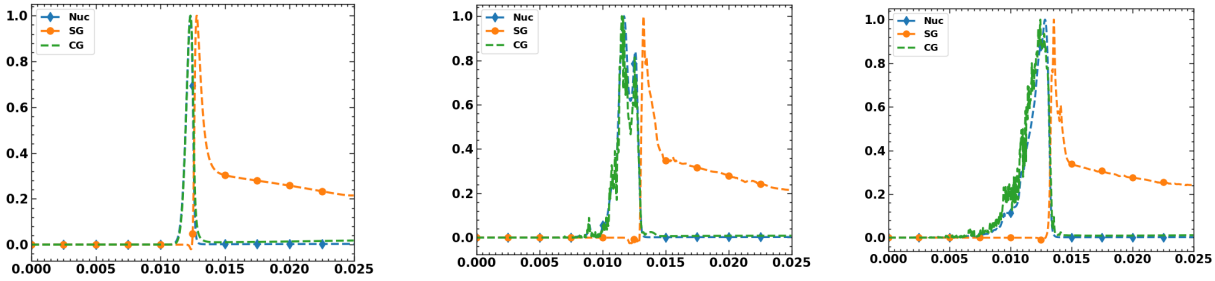

Figure 39. Normalized nucleation (Nuc), coagulation (CG) and surface growth (SG) source terms.

The comparison of nucleation and surface growth terms is shown in Figure 40 for $\phi = 1.8$. The surface growth adds more soot mass compared to nucleation under laminar as well as turbulent conditions. The surface growth source terms are further analyzed to understand contributions from surface growth due to C_2H_2 additions and surface oxidations due to O_2

and OH and are shown in Figure 41 for $\phi = 1.8$. The soot mass addition due to C_2H_2 is almost three times more dominant than O_2 and OH radicals. The oxidation by OH molecules is four times higher than the O_2 molecule.

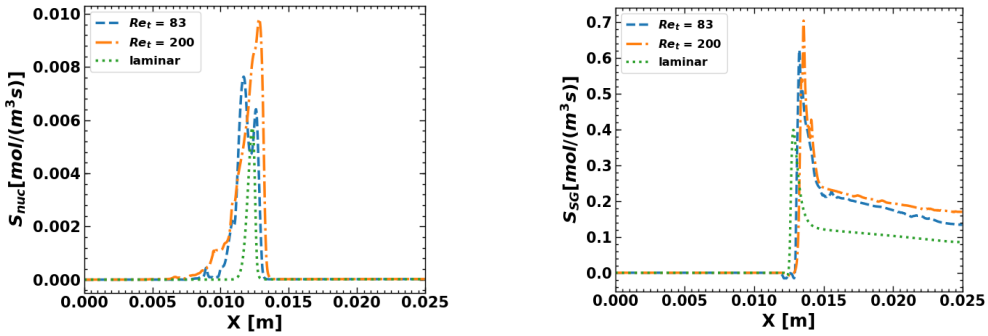

Figure 40. Comparison of contribution from nucleation and surface growth.

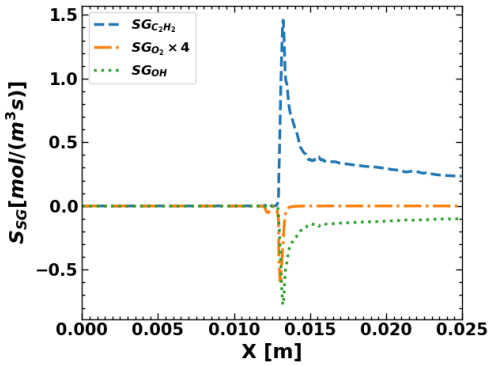

Figure 41. Comparison of contribution from C_2H_2, O_2, and OH for soot surface growth and oxidation.

4.4 Coupling RTRC PM-ROM within Soot Models at GT

In this section, we specifically focused on coupling the RTRC PM-ROM model within our soot modeling framework. We specifically look at the propagation of a laminar flame through a rich premixed gas phase mixture under combustor-relevant conditions. The physics of soot formation in this scenario is depicted in the schematic shown in Figure 42. Using this setup, we compared baseline Lindstedt model with RTRC PM-ROM and also the role of aggregation models in the post-flame environment. In this configuration, a premixed reactant mixture enters the 1D domain from the left side and burns at the flame front. Due to an insufficient amount of oxidizer, the fuel-rich mixture cannot completely combust, leading to the decomposition of leftover fuel into soot. Various stages of soot formation occur behind the flame. Immediately after the flame front, influenced by the kinetic model, nucleation, surface growth, and oxidation processes initiate the formation of soot, which continues to aggregate as it progresses downstream.

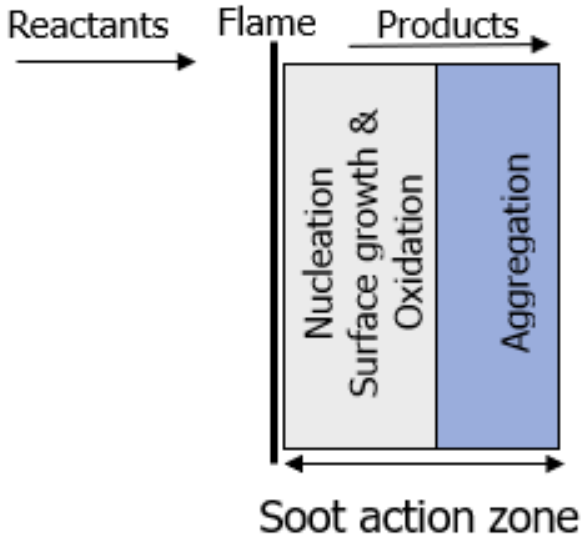

Figure 42. Schematic of Laminar Premixed Flame.

As illustrated in Figure 43, the PM-ROM model predicts slightly less soot accumulation than the Lindstedt model (similar to the observations in Task 1 at RTRC). We also explored the sensitivity of incorporating an aggregation model, which helps characterize the structure of soot aggregates forming behind the flame, as depicted in Figure 44. The baseline model posits that aggregation effects commence once the primary particle reaches a critical diameter of 27 nm, with a fractal dimension of 1.8. Incorporating the aggregation model enhances the rate of particle coagulation, leading to a decrease in soot aggregate density. However, as aggregation increases the overall surface area available for soot reactions, it consequently raises the soot volume fraction. The aggregation model specifically influences the sizes of the particles formed behind the flame; without it, the model predicts large, spherical particles, whereas with aggregation, a cluster of soot aggregates composed of primary spherical particles is predicted.

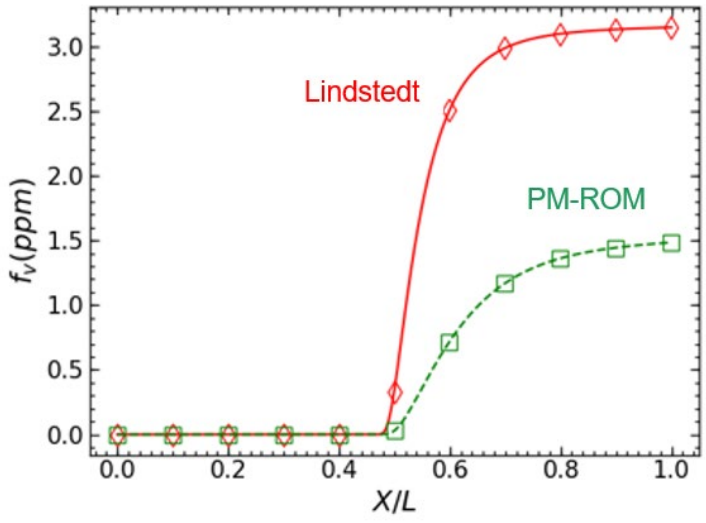

Figure 43. Soot volume fraction behind the laminar flame.

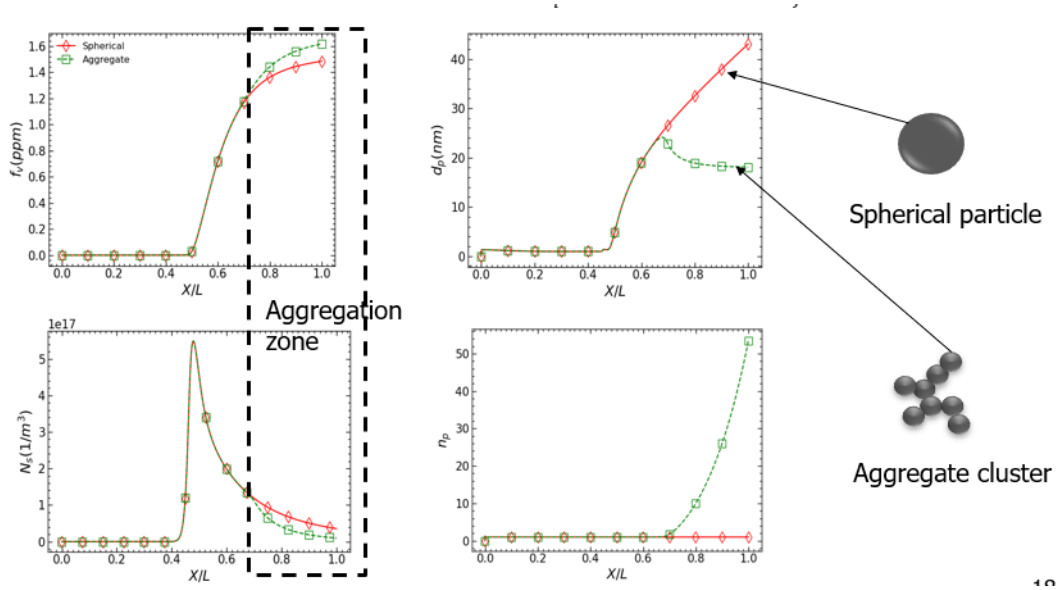

Figure 44. Aggregate characteristics of non-volatile particulate matter (nvPM) formed behind the flame.

4.4 Apply Moment Soot Models at GT to RQL Spray Flames

In the remainder of the project work, the modeling framework is applied to study soot formation in a realistic RQL spray combustor. The computer-aided design (CAD) model of the rig investigated in the Year 3 effort is shown in Figure 45a. The RQL burner simulated in GT is a subsection (only one swirler) and is represented in Figure 45b.

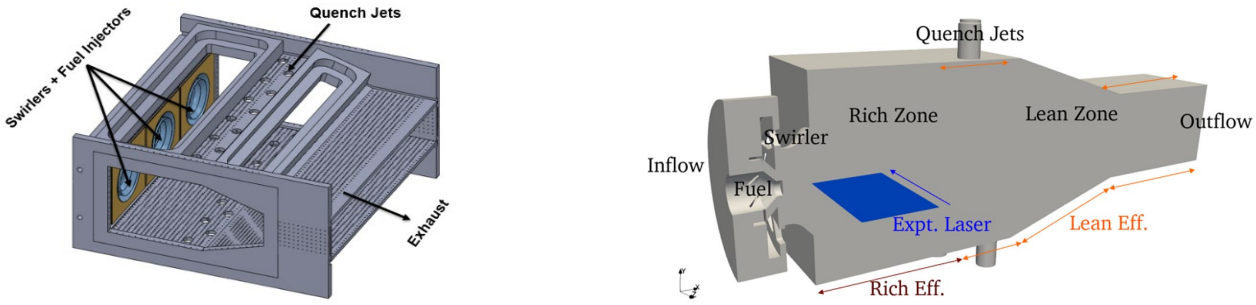

(a) Three-swirler RQL experimental rig (b) Model single-injector combustor with periodic BC

Figure 45. Computational aspects of the sector rich-burn quick-mix lean-burn (RQL) rig investigated in the current work.

In summary, the computational domain from the inlet plenum to the outlet duct is considered. The overall components of the combustor consist of the swirler, fuel injector, quench jets, effusion surfaces, and the outlet duct. The main combustor has the primary rich zone from the dump plane to the quench jets and the secondary lean burn zone post-quench jets. The overall combustor operates at a pressure of 6.8 atm and the preheated air at a temperature of 600K is supplied through different inlets such as the primary inflow, quench jets, and the effusion holes along the walls of the rich primary and lean secondary zones of the combustor. We have primarily investigated two cases corresponding to lower fuel-air ratio (case A, $\phi_g = 0.12$) and higher fuel-air ratio (case B, $\phi_g = 0.2$).

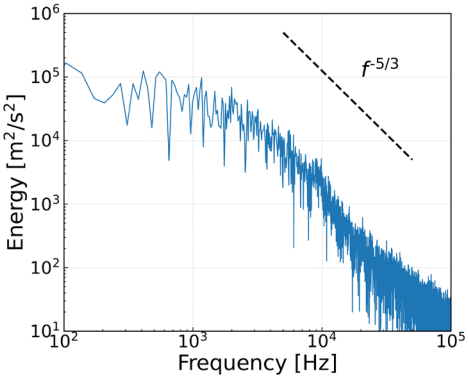

Figure 46. Current grid demonstrates Turbulent Kinetic Energy cascade over two orders of magnitude scales.

The computational domain is discretized using 6.3 million finite-volume cells. A multi-block structured grid with hanging nodes is generated to handle the geometric complexities of the combustor. Shear layers are resolved with minimum grid points of 0.25 mm - 0.7 mm consistent with previous LES simulations (Panchal & Menon, 2022). Swirlers have 10 points along their span. The grid quality is on average above 0.9 with a minimum value of 0.7 mainly near dilution jets and geometrically complex swirled regions. The stretching ratio of 1.01 is applied on average with a maximum value of 1.2 near the outlet channel and the inlet plenum where no complex physics occurs. The kinetic energy spectra, as shown in Figure 46, demonstrates that the current grid captures 5/3rd energy cascade typically observed in turbulent flows.

The parts that are stitched together with hanging nodes use an interpolation scheme of the same order of accuracy as the numerical scheme. The geometry is further split into 5,141 blocks. Characteristic-based constant mass inflow boundary conditions are used at the primary inflow as well as inflow for quench jets. Periodic boundary conditions are used in the z-direction (spanwise-direction) as the current work focuses only on the single section of the multi-sector grid. At the outflow, the domain is extended by 30% of the combustor length, and a relaxing sponge boundary condition is applied. Small effusion holes are present throughout the walls in the primary and secondary zones of the combustor for wall cooling. Such holes are difficult to resolve in LES and hence are modeled using an effusion boundary condition. The air split for the combustor is 18% from the dome face (resulting in the equivalence ratios of 0.66 and 1.14 in the primary zone of the combustor), 44% from the two rows of quench holes, 7% from effusion cooling holes in the rich-burn region, and 19% for the effusion cooling holes in the lean-burn, taper, and exhaust regions.

In the current work, the numerical scheme for the gas phase is of second-order accuracy in time while a hybrid scheme for spatial discretization is employed, which dynamically switches between a second order-accurate MacCormack central scheme and a third order-accurate Monotone Upstream-centered Schemes for Conservation Laws (MUSCL) scheme. A fourth order-accurate Runge-Kutta method for time integration is used for the Lagrangian phase.

Due to the absence of corresponding experimental data, the non-reacting flow features are only qualitatively illustrated in Figure 47 and discussed here. The radial swirlers generate a strong swirling motion with a swirl number of approximately 1.6 near the combustor dump plane, which exceeds the critical threshold (typically 0.6 for such flows). This high swirl intensity induces a recirculating region downstream, known as the vortex breakdown bubble (VBB), marked by the solid blue line in Figure 47(a,b). The VBB arises primarily from an adverse pressure gradient and is characterized by a region of negative axial velocity, as seen in the centerline velocity profile (Figure 47c). This recirculation gives rise to toroidal central recirculation zones (CRZ) adjacent to the high-shear layers. Qualitatively the non-reacting field exhibits various regimes typical of swirling flows.

Figure 47c also denotes the length of VBB about 0.36 times the overall combustor length from the dump plane. Additionally, obtained turbulence intensity ($q' = \frac{1}{3}\sqrt{u'^2_{x,rms} + u'^2_{y,rms} + u'^2_{z,rms}}$) suggests that peak turbulence intensity increase in magnitude with peaks near the edge of VBB and then decreases in magnitude along the length of the combustor. The recirculation zones are also observed to be asymmetric (see Figure 47b) due to two main reasons. First, the dilution jets are arranged along the top and bottom walls of the combustor in a zigzag pattern, resulting in inherently asymmetric

interactions with the CRZs as seen in Figure 47b. The quench jets bend differently as a result of their interactions with the crossflow from the primary zone and with dilution jets entering from the opposite side, further enhancing the asymmetry. Additionally, preheated air effuses along the lower experimental combustor wall and pushes up the lower CRZ whereas the top glass window does not include such effect.

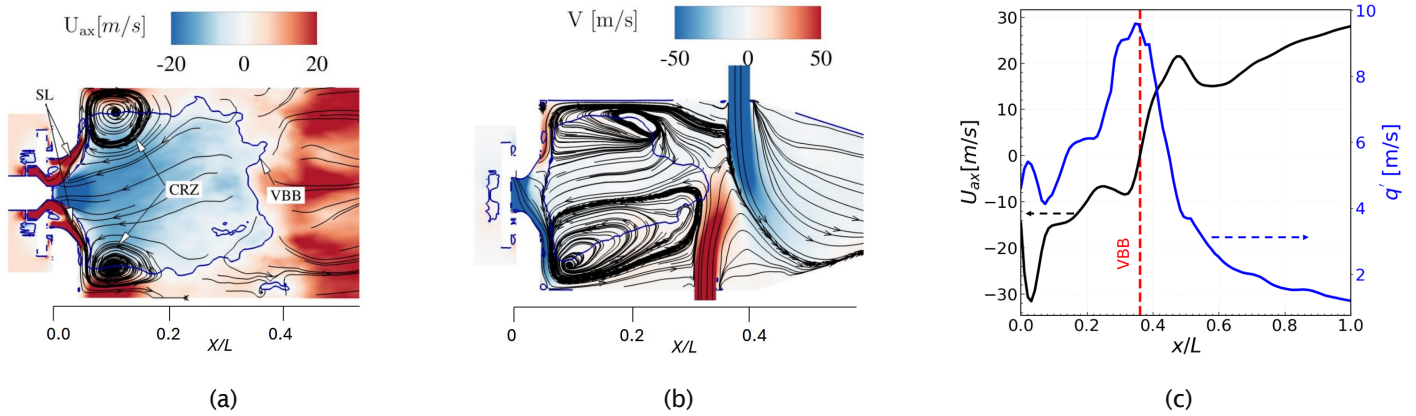

(a) (b) (c)

Figure 47. Swirling flow features showing the presence if recirculating zones in the region of interest.

Liquid fuel is injected from the swirled fuel nozzle, and the surrounding high-speed air assists the injected fuel atomization. Such liquid fuel goes through a primary and secondary breakup before the droplets are small enough to vaporize and burn. However, it is not practical to resolve such near-injector dynamics of atomization and since the goal here is primarily to study overall soot formation in the primary zone, Lagrangian point particles are injected downstream of the actual injector with an assumed log-normal distribution. Such assumptions behind the treatment of spray can certainly have an impact on the soot formation but as per our knowledge, have not been investigated in literature yet. The qualitative features of this spray flame are shown in Figure 48.

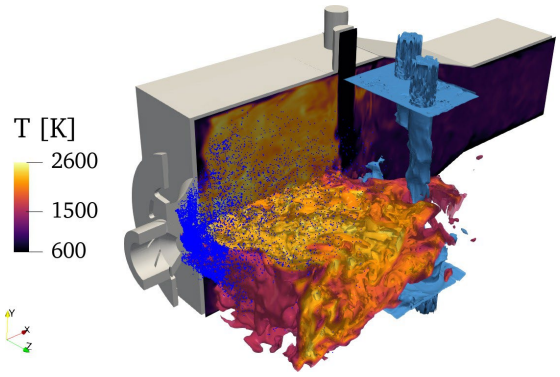

Figure 48. Qualitative visualization of spray droplets (blue color), quench jets (sky-blue isosurfaces) and temperature field iso-surfaces as well as slice through center of dilution jets.

Under identical operating conditions, with variations only in the fuel injection flow rates, case A and case B exhibited approximately 0.065 million and 0.11 million droplets, respectively, after reaching a quasi-steady state. The comparisons of unsteady flame temperature (top halves) and OH species fields (bottom halves) resulting from the combustion of vaporized fuel are shown in Figure 49. The overall combustion behavior shows qualitative similarities in both cases. As shown by the temperature contours, the central region (the recirculating region of the VBB) is hot in both cases. This recirculation promotes further vaporization of the incoming spray and acts as an aerodynamic flame holder. Additionally, both the contours of OH species and temperature are highly wrinkled due to interactions with background turbulence. The OH concentrations field shows local extinction spots, which are also observed in other swirl-stabilized spray flames. The

secondary zone is relatively cold compared to the primary zone, due to the sudden mixing of the quench jet air with the hot products from the primary zone. Despite these qualitative similarities, notable differences are also observed. First, the temperature in the primary zone of the combustor is higher in case B compared to case A. This trend persists in the secondary zone of the combustor post-quench jets. A similar pattern is evident in the unsteady OH field, where case B showed denser OH radical concentrations in the primary zone than case A.

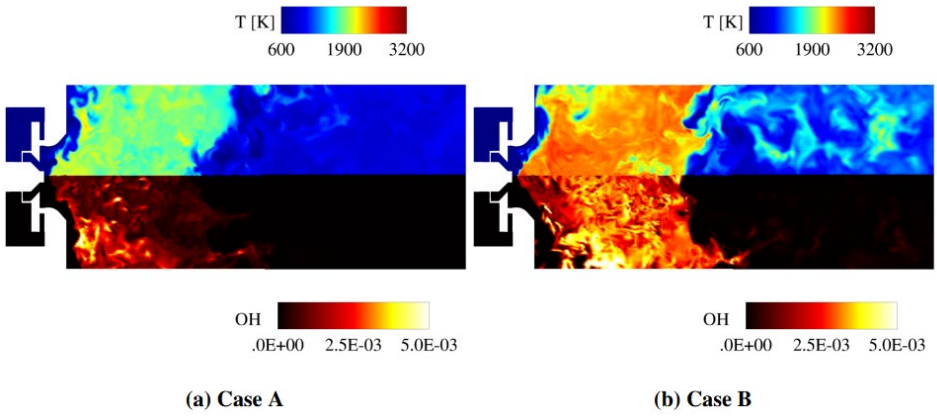

Figure 49. Reacting flow-field comparison of temperature and OH-mass fraction between the investigated cases.

The instantaneous and time-averaged soot presence are compared against the experimental visualizations, as shown in Figure 50, for the two fuel-air ratios investigated in this work. The top set of experimental images shows the LII signals captured by a Shimadzu HPV-X2 high-speed camera using a Spectra-Physics® Quanta-Ray® Pro-250 Nd:YAG laser. Due to the sensitivity of soot estimations to measurement techniques and the modeling uncertainties in soot processes, achieving accurate quantitative validation of LES soot predictions against experiments is challenging, and hence normalized locations of soot presence are compared between the two cases. First, the overall soot formation increases from case A to case B, consistent with experimental observations. For case A, the central recirculating region, is almost completely devoid of soot. Soot seems to be mainly concentrated along the shear layers. On the contrary, a significant soot presence is observed in case B and shows better spatial alignment with the experimental results. There is a slight discrepancy in the transverse location of peak soot on the left side and an overall underprediction of soot downstream of X > 0.02 m compared to experimental observations. However, such discrepancies have also been observed in gas-phase RQL sooting flames, even with state-of-the-art soot modeling. Nevertheless, based on qualitative visual comparisons, the overall influence of the equivalence ratio on soot formation appears to be reasonably captured in the simulations, which was the primary objective of the current analysis. The underlying mechanism behind these observations is analyzed by comparing further the distribution of different soot processes involved in the soot formation and destruction.

® Spectra-Physics and Quanta-Ray are registered trademarks of Newport Corporation, Irvine, California.

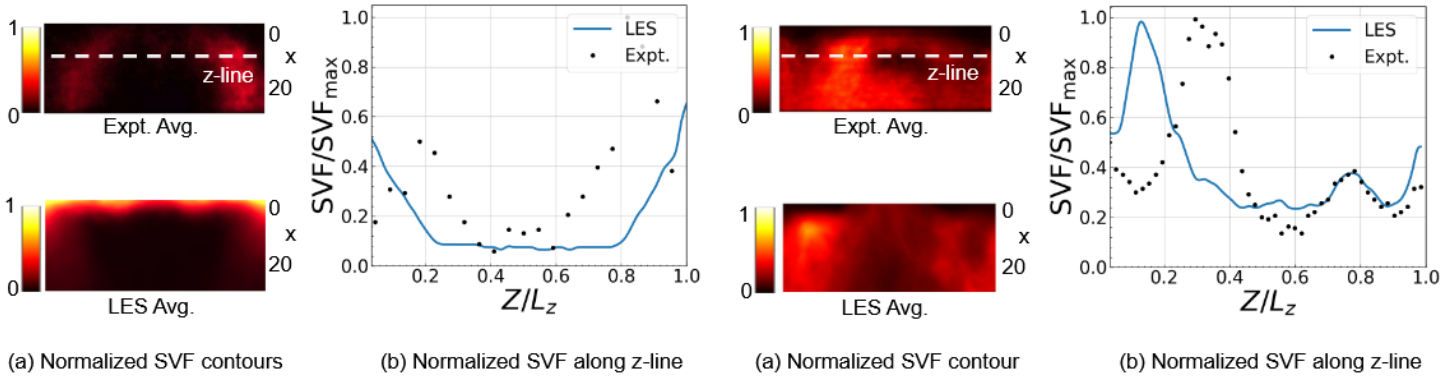

Figure 50. Soot volume fraction field is compared with the experimental data for Case A and Case B.

Figure 51 compares the time-averaged spatial distributions of the nucleation, surface growth, condensation, and oxidation source terms for both operating conditions, as these processes collectively determine the evolution of the soot. Contours of the source-term magnitudes are included to highlight the quantitative differences between the two cases. In addition, Figure 52 presents the mass fractions of key soot precursor species to compare their relative availability for the underlying soot formation and oxidation pathways. Soot inception (Figure 51a) occurs near the fuel injector, where the fuel-air mixture is very rich, and dense pockets of A2 exist (Figure 52b). This nucleation persists along the shear layers, though its intensity decreases as the fuel-air mixing progresses. Condensation closely follows nucleation, exhibiting a similar trend due to the involvement of the same PAH species in both processes. Quantitative comparisons of isolines from Figure 51a and Figure 51c reveal that both nucleation and condensation processes are higher in case B than in case A due to overall higher PAH species formed. In addition, for case A, as shown in Figure 51b, surface growth source terms are very low compared to case B. Especially, the surface growth begins immediately after the onset of inception zones, and its influence is only confined along the shear layers. This behavior is associated with the overall low concentrations of C_2H_2 as shown in Figure 52c. Moreover, the soot particles formed undergo oxidation and hence show less tendency to intermittently trap in recirculation zones at lower global fuel-air ratio. A similar mechanism is initially observed in case B, where surface growth and oxidation processes start following the inception and condensation zones. However, the overall magnitudes of surface growth in Figure 51b are higher in case B than in case A, consistent with elevated concentrations of C_2H_2. This sustained growth persists not only along the shear layers but also within the inner recirculation zones, where longer residence times further promote soot growth. The increased surface area resulting from surface growth, combined with the dense presence of oxidizer, leads to higher oxidation rates further downstream from the combustor dump plane, primarily within the primary zone. These observations suggest that soot formation in the primary zone is dominated by surface kinetics rather than inception.

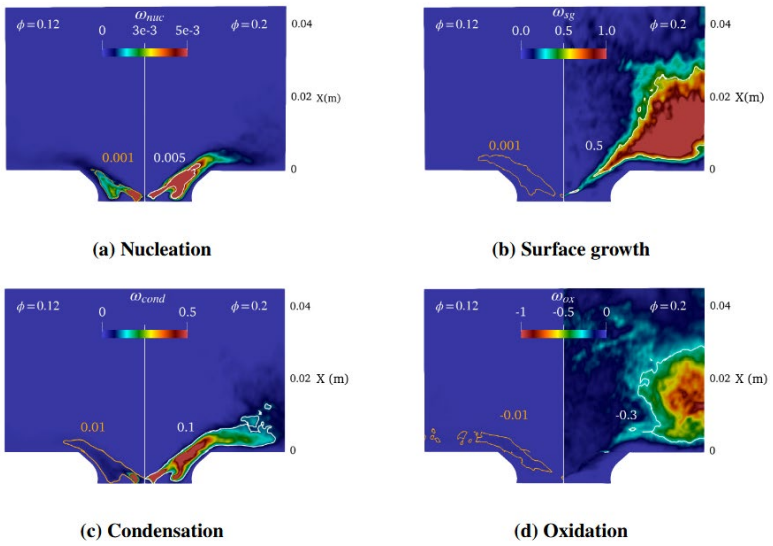

Figure 51. Comparative assessment of time-averaged soot source terms (kg/m3.s) between case A (left half) and case B (right half). Lines represent the order of magnitude of source terms for respective cases.

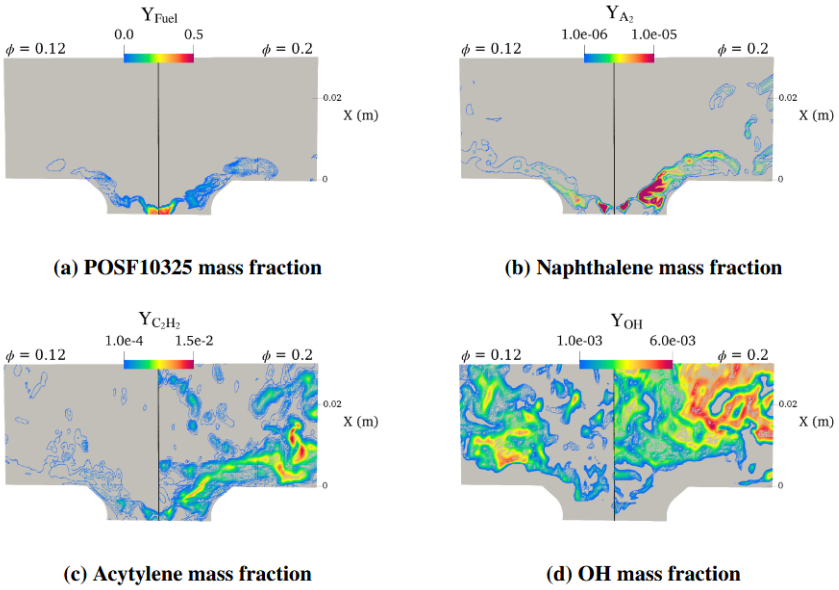

Figure 52. Comparative distribution of vaporized fuel (a) and key precursor species (b), (c), and (d) involved in soot formation reactions for the two investigated cases: case A (left half) and case B (right half).

4.5 Modeling Coupled Detailed Kinetics in the Soot Model

The systematic investigation of kinetic and nucleation model effects is computationally expensive to perform within the full 3D LES. Therefore, in the current work, a CRN model is employed in which the hydrodynamic field is assumed frozen, and only the effects of chemistry are solved by constructing a network of reactors that are connected via mass flow controllers.

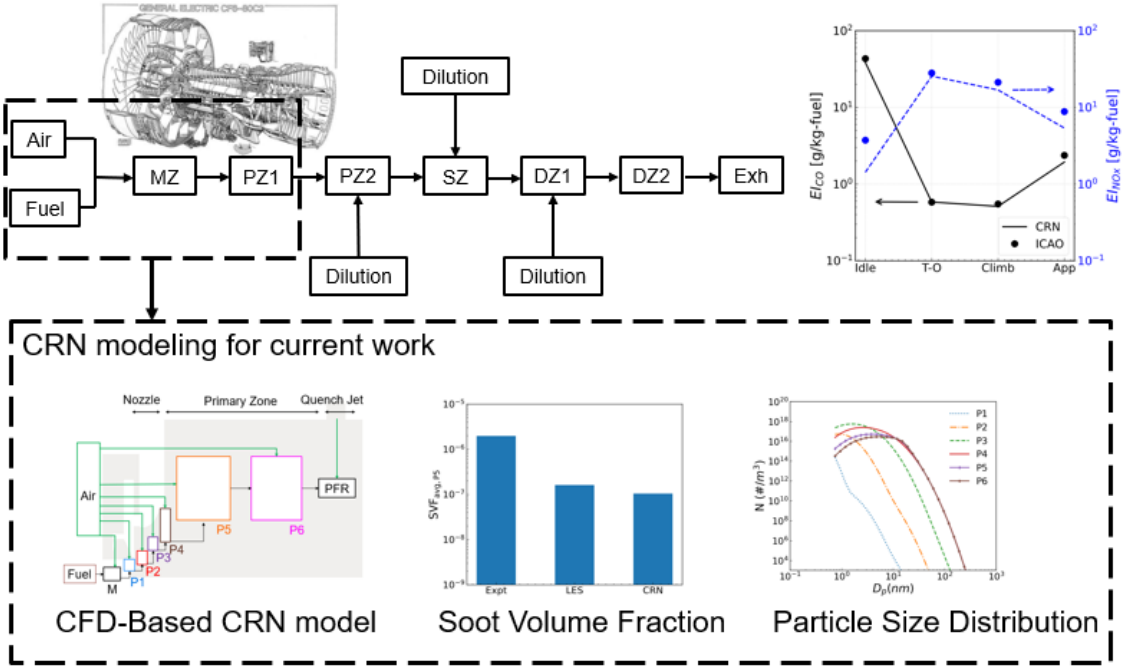

Figure 53. Chemical Reactor Networks (CRN) modeling framework employed in the current work. The top figures show CRN model predictions for rich-burn quick-mix lean-burn (RQL) combustors against the International Civil Aviation Organization (ICAO) emission databank. The bottom figures show a refinement of this CRN model for the primary zone of the RQL combustor investigated in this work. CFD: computational fluid dynamics.

We also exploited the capabilities of the CRN model coupled with Dakota (Figure 54 for overall framework) to perform a comprehensive uncertainty analysis of its predictions (Karpe & Menon, 2025). This analysis aimed to understand the response of the baseline soot model to input uncertainties through forward uncertainty quantification (UQ) analysis, while sensitivity analysis was performed to assess the relative contribution of each process to the overall predictive uncertainties. Here, the results of the local sensitivity analysis, which are more relevant to the current work, are reported.

® General Electric is a registered trademark of General Electric Company, Evendale, Ohio.

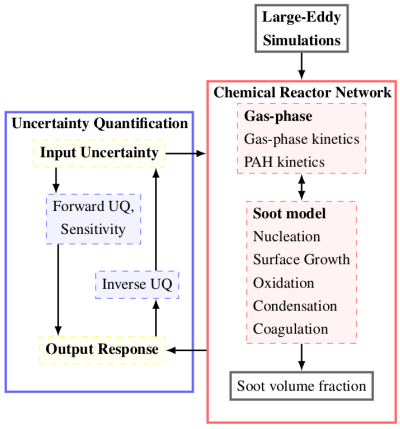

Figure 54. Uncertainty analysis framework to investigate modeling sensitivities of baseline soot model. UQ: uncertainty quantification.

As can be seen from Figure 55, normalized local sensitivity indices are plotted first. Such indices generally provide an intuitive representation of how local perturbations in the baseline rates influence the overall soot formation or depletion. The positive value of such an index suggests that an increase in the baseline rate of the process promotes soot formation, whereas the negative value implies it contributes to soot depletion. The local sensitivity analysis reveals the nucleation, growth, and condensation process consistently show positive sensitivity indices, whereas the oxidation has a negative local index. Coagulation appears to have a marginal impact on the total soot mass. Furthermore, if we compare the trends of these reactors, the P3 reactor, located upstream of the primary zone, showed the highest sensitivity to PAH-based processes. In contrast, further downstream, P4-P6 reactors display stronger sensitivity to the growth and oxidation processes.

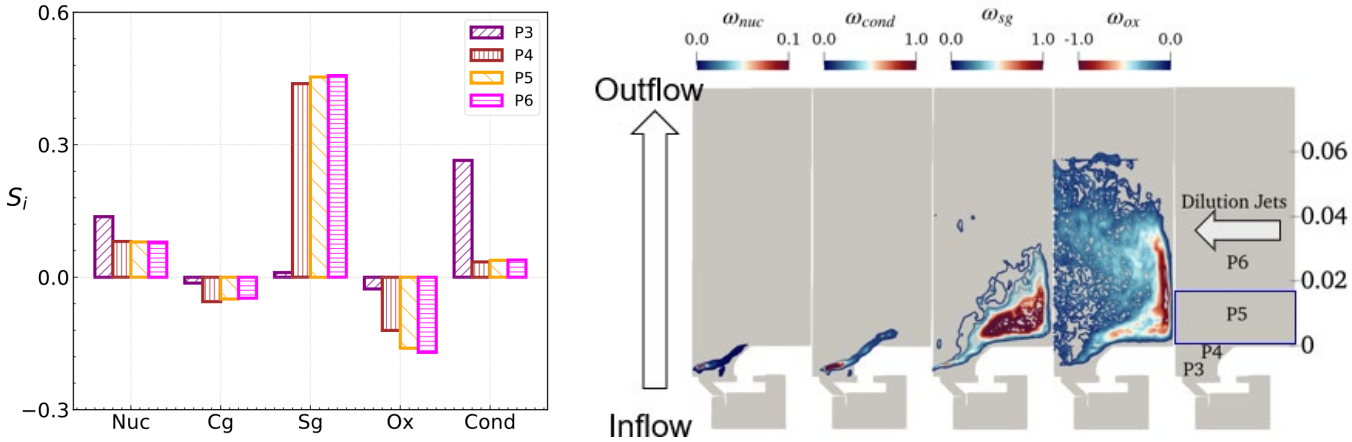

Figure 55. (a) Influence of soot subprocesses in different reactors using the uncertainty quantification-Chemical Reactor Network (UQ-CRN) framework. (b) Presence of these processes from large eddy simulation (LES) highlighting the consistency between the both. Overall the relative dominance of each of the soot processes is tracked along the spatial extent of the combustor.

These findings are further supported by visualizing the presence of these processes in different zones of the combustor. As can be seen, the nucleation and condensation processes influence a localized region within the nozzle, primarily along the shear layers, while the growth and oxidation processes are more prominent in the primary zone of the combustor. This suggests that these nanoparticles form in the shear layer and undergo further growth as they are transported in the inner

recirculation zone of the primary zone. Within the primary zone, the influence of oxidation is observed to increase, and this possibly occurs due to the enhanced mixing of the primary zone-rich mixture with cold air entering through the dilution jets, gradually making the mixture lean.

Finally, this local influence of different processes is used in the next part of the work to understand the effects of changing the gas-phase chemistry, nucleation models, and growth kinetics at these reactors (for example, the rates of nucleation and condensation processes in the P3 reactor, whereas growth and oxidation processes in the P5 reactor) and overall soot predictions in the P5 reactor. The following sections present a brief account of such effects.

First, the effects of gas-phase kinetics on overall predictions are assessed by varying the gas-phase mechanisms. The three different mechanisms investigated in this work are listed in Table 3. The skeletal mechanism by Gallen (2023), was also used in the LES simulations, while the second mechanism, developed by Wang et al. (2018), combines the HyChem mechanism with the KAUST mechanism. The third mechanism, referred to as the RTRC mechanism, was developed through collaborations with the RTRC kinetics group and integrates the HyChem mechanism with the CalTech-Force mechanism. Although the detailed gas-phase mechanisms provide a wide range of PAH species that can be considered for nucleation, to isolate the effects of the gas-phase kinetics, the same soot model—namely, the baseline soot model—is coupled with all three mechanisms. These effects are presented in Figure 56.

Table 3. Different gas-phase kinetics mechanisms investigated in this work.

Mechanism	# of species	PAH Mechanism
Gallen	45	Bisetti
Wang	210	KAUST
RTRC	222	Caltech

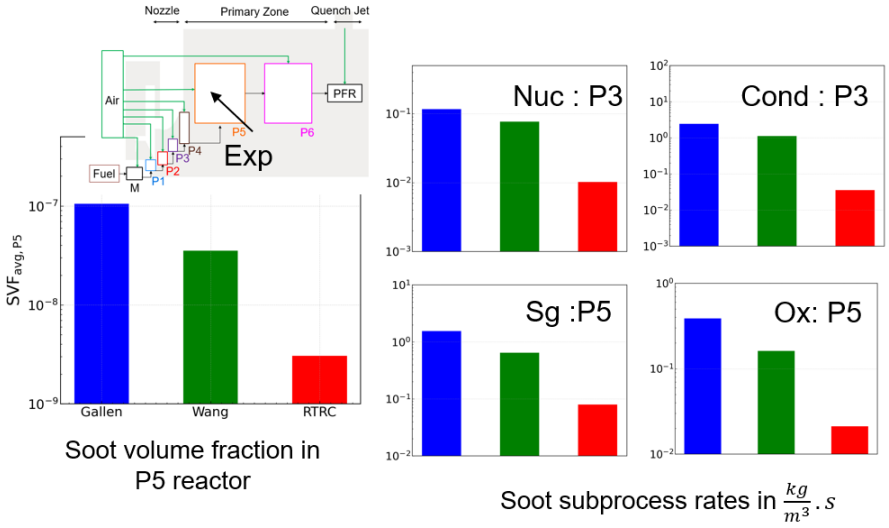

Figure 56. Effects of detailed gas phase mechanism on primary zone soot predictions of rich-burn quick-mix lean-burn (RQL) system.

As seen in Figure 56, both detailed mechanisms generally predict slightly lower soot levels compared to the skeletal Gallen mechanism. The Wang detailed mechanism still shows reasonable agreement with the Gallen mechanism, whereas the RTRC mechanism predicts soot concentrations approximately an order of magnitude lower than those predicted by the other two mechanisms. This discrepancy is likely due to the lower concentrations of soot precursor species predicted by the detailed mechanisms, resulting from the enhanced breakdown of C_2H_2 and naphthalene into heavier PAH species. This

trend is evident from the peak rates of the individual processes responsible for soot formation and oxidation. In particular, the RTRC mechanism predicts condensation and growth rates approximately an order of magnitude lower than those predicted by the other detailed and reduced mechanisms. These results suggest that soot predictions are highly sensitive to the choice of gas-phase kinetics, as the mechanism directly influences the individual process rates through species concentrations.

The use of a detailed gas-phase mechanism also enables the investigation of various nucleation models, particularly those involving heavier PAH species beyond naphthalene. In this work, five such nucleation models are examined, as summarized in Table 4. The first two models are based on nucleation involving naphthalene (A_2). In general, PAH species form stable dimers through collisions, which are characterized by an efficiency parameter (γ_{PAH}). These two models explore the influence of incorporating this efficiency parameter. In the first model, the sticking coefficient for naphthalene collisions follows the value recommended by Blanquart et al. (2009), whereas in the second model, the sticking efficiency is assumed to be unity. The next set of models involves nucleation based on pyrene. Lastly, the M5 model incorporates inputs from nucleation studies conducted at UM. As the parameters in this model have already been calibrated to account for sticking efficiency, no additional variation in this parameter is investigated.

Table 4. Different nucleation mechanisms investigated in this work.

-	PAH	γ_{PAH}
M1	Naphthalene (A_2)	0.0011
M2	Naphthalene (A_2)	1.0
M3	Pyrene (A_4)	0.025
M4	Pyrene (A_4)	1.0
M5	Benzo-pyrene (A_4R_5)	1.0

As shown in Figure 57, the incorporation of nucleation effects can significantly influence soot predictions. Generally, the naphthalene-based model predicts higher overall soot levels compared to the pyrene-based models, primarily due to the lower concentrations of pyrene relative to naphthalene. Furthermore, since nucleation is the initial step in the soot formation process, variations at this stage can have a substantial impact on the subsequent processes. To further investigate this, the peak source rates of condensation, surface growth, and oxidation are also plotted. Increased nucleation rates typically result in a greater number of incipient soot particles, thereby enhancing subsequent condensation, growth, and oxidation processes through the increased availability of surface area. Since the overall rates of nucleation are generally smaller than those of growth and condensation, the influence of nucleation is primarily indirect, exerted through its effect on subsequent processes rather than by directly contributing to soot mass.

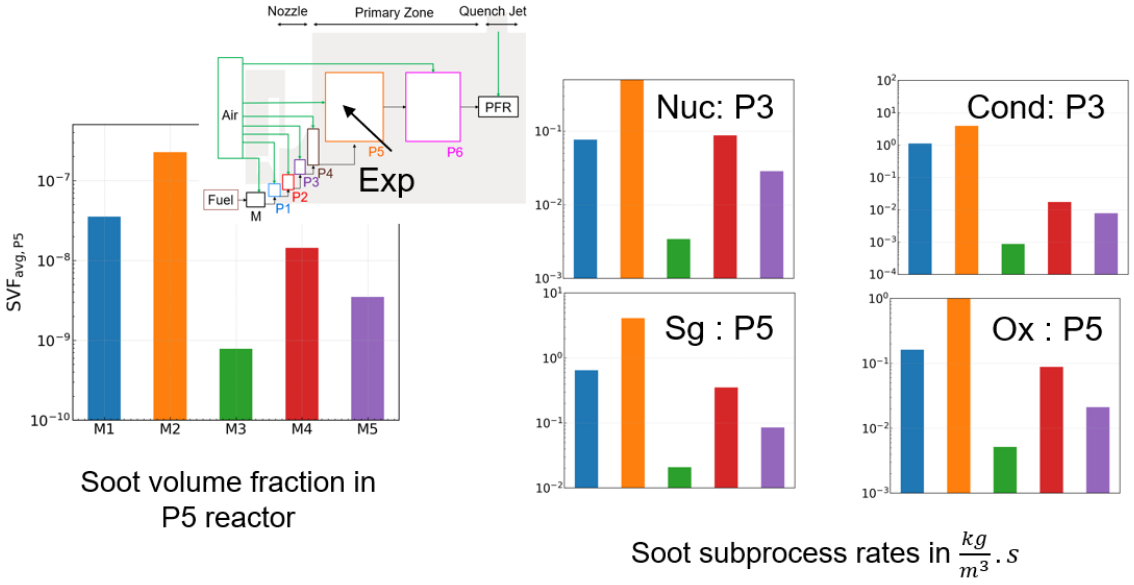

Figure 57. Effects of different nucleation mechanisms (M5 represents the nucleation mechanism obtained from the University of Michigan) on primary zone soot predictions of rich-burn quick-mix lean-burn (RQL) system.

After understanding the effects of the gas-phase kinetics and nucleation model, the effects of growth modeling are systematically investigated by changing the growth kinetics. For consistency, the baseline soot model is kept where nucleation is assumed to occur via naphthalene dimerization whereas the reduced gas-phase kinetics is used. In the current work, three different growth kinetics models are investigated: (1) Kazakov et al. (1995), (2) Appel et al. (2000), and (3) Blanquart et al. (2009). From the overall soot volume fractions predicted for P5 reactors, it seems that the surface growth reaction mechanism plays a vital role. The Kazakov mechanism produced the least soot volume fractions whereas the Blanquart mechanism predicted the highest soot volume fractions with the Appel-Bockhorn-Frenklach (ABF) mechanism in between. To delineate these effects further, the source rates of these processes at their respective peak locations are also compared. As can be seen from Figure 58, as expected, the nucleation and condensation processes didn't have much influence on such variation in surface growth kinetics as they occur before the surface growth effects start dominating. The major influence of varying surface growth kinetics is observed on the surface source rates in the P5 reactor. At the same time, the Blanquart mechanism also predicted slightly lower oxidation rates as compared to the Kazakov and ABF mechanisms, further enhancing soot formation.

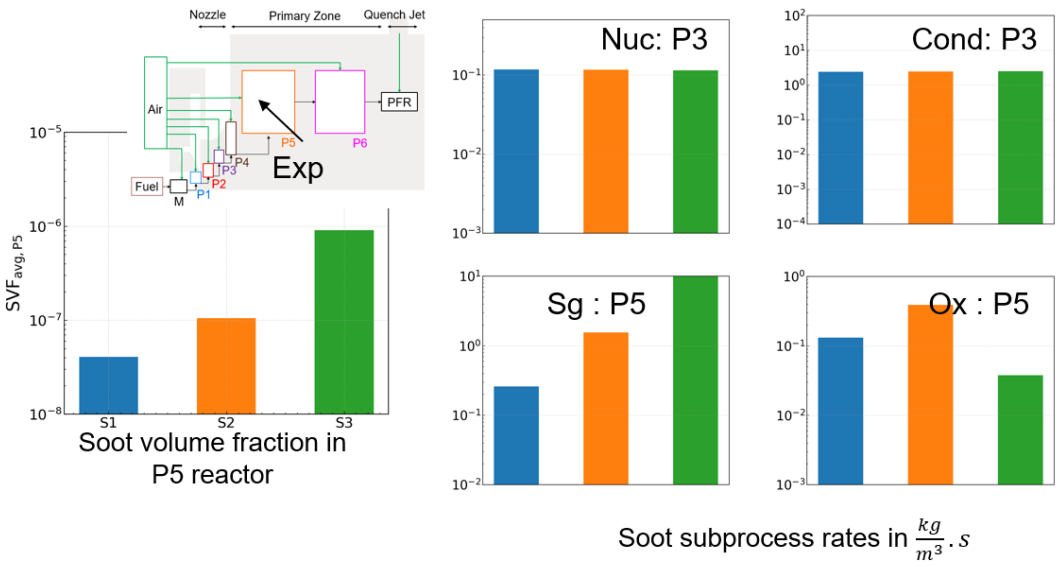

Figure 58. Effects of varying growth kinetics on primary zone soot predictions of rich-burn quick-mix lean-burn (RQL) system.

Major Accomplishments

- Established the baseline MOM-based soot modeling framework, both in standalone form and integrated within LES for canonical flame configurations.
- Quantified the sensitivity of soot predictions (soot volume fraction) to gas-phase kinetics, nucleation models, and aggregation parameters, and shared these findings with collaborative partners.
- Developed a standalone LEM-based strategy to upscale soot source terms for use at LES-resolved turbulence scales.
- Performed LES simulations of a sooting RQL spray combustor at two operating conditions and compared results against FAA ASCENT Project 070 data.
- Incorporated detailed gas-phase kinetics from RTRC and the nucleation model from UM into the MOM soot framework and evaluated their effects relative to variations of the baseline soot models.

Publications

Peer-Reviewed Journal Publications

Karpe, S., & Menon, S. (2022). Numerical Simulations of Soot Formation in Turbulent Premixed Flames of Jet Fuels. *75th Annual Meeting of the APS Division of Fluid Dynamics, 67*(19).

Karpe, S., & Menon, S. (2025). Modeling uncertainties in primary zones soot predictions for rich-quench-lean combustion system. *Proceedings of Combustion Institute, 41*, 105805.

Presentations

Karpe, S., & Menon, S. (2023, January). Model Simulations of Soot Formation due to PAH Kinetics from Mixing Layers of Jet-A Fuels. (AIAA-2023-2690). *AIAA SciTech 2023 Forum*, National Harbor, Maryland.

Karpe, S., & Menon, S. (2025, January). Large-Eddy Simulations of Soot Formation and Dispersion in Rich-Burn Quick-Mix Lean-Burn (RQL) Spray Combustor (AIAA-2025-2484). *AIAA SciTech 2025 Forum*, Orlando, Florida.

Karpe, S., & Menon, S. (2026). Large-Eddy Simulations of dilution jet effects on rich-quench-lean spray flame. *AIAA SciTech 2026 Forum*.

Outreach Efforts

None.

Awards
None.

Student Involvement
One PhD student, S. Karpe, was involved in this work.

Plans for Next Period
None.

References

Appel, J., Bockhorn, H., & Frenklach, M. (2000). Kinetic modeling of soot formation with detailed chemistry and physics: Laminar premixed flames of C2 hydrocarbons. *Combustion and Flame*, *121*(1-2), 122-136.

Attili, A., Bisetti, F., Mueller, M. E., & Pitsch, H. (2014). Formation, growth, and transport of soot in a three-dimensional turbulent non-premixed jet flame. *Combustion and flame*, *161*(7), 1849-1865.

Bisetti, F., Blanquart, G., Mueller, M. E., & Pitsch, H. (2012). On the formation and early evolution of soot in turbulent nonpremixed flames. *Combustion and Flame*, *159*(1), 317-335.

Blanquart, G., Pepiot-Desjardins, P., & Pitsch, H. (2009). Chemical mechanism for high temperature combustion of engine relevant fuels with emphasis on soot precursors. *Combustion and Flame*, *156*(3), 588-607.

Brown, N.J., Revzan, K.L., & Frenklach, M. (1998). Detailed kinetic modeling of soot formation in ethylene/air mixtures reacting in a perfectly stirred reactor. Symp*osium (International) on Combustion, 27*, 1573–1580.

El-Asrag, H., & Menon, S. (2009). Large eddy simulation of soot formation in a turbulent non-premixed jet flame. *Combustion and Flame, 156*(2), 385–395.

El-Asrag, H., Lu, T., Law, C. K., & Menon, S. (2007). Simulation of soot formation in turbulent premixed flames. *Combustion and Flame, 150*(1-2), 108–126.

Frenklach, M. (2002). Method of moments with interpolative closure. *Chemical Engineering Science, 57*(12), 2229–2239.

Gallen, L., Riber, E., & Cuenot, B. (2023). Investigation of soot formation in turbulent spray flame burning real fuel. *Combustion and flame*, *258*, 112621.

Guo, H., Liu, F., & Smallwood, G. J. (2004). Soot and NO formation in counterflow ethylene/oxygen/nitrogen diffusion flames. *Combustion Theory and Modelling*, *8*(3), 475

Karpe, S. B., & Menon, S. (2025). Modeling uncertainties in primary zone soot predictions for a rich-quench-lean combustion system. *Proceedings of the Combustion Institute*, *41*, 105805.

Kazakov, A., Wang, H., & Frenklach, M. (1995). Detailed modeling of soot formation in laminar premixed ethylene flames at a pressure of 10 bar. *Combustion and Flame*, *100*(1-2), 111-120.

Langer, R., Mao, Q., & Pitsch, H. (2023). A detailed kinetic model for aromatics formation from small hydrocarbon and gasoline surrogate fuel combustion. *Combustion and Flame, 258*, 112574.

Leung, K. M., Lindstedt, R. P., & Jones, W. P. (1991). A simplified reaction mechanism for soot formation in non-premixed flames. *Combustion and Flame, 87*(3-4), 289–305.

Menon, A. V., Lee, S. Y., Linevsky, M. J., Litzinger, T. A., & Santoro, R. J. (2007). Addition of NO2 to a laminar premixed ethylene–air flame: Effect on soot formation. *Proceedings of the Combustion Institute*, *31*(1), 593-601

Menon, S., & Ranjan, R. (2016). Spray Combustion in Swirling Flow (Ch. 12). In *Coarse-Grained Simulation and Turbulent Mixing*. Cambridge University Press.

Menon, S., & Kim, W. (1996, January). High Reynolds number flow simulations using the localized dynamic subgrid-scale model (AIAA 1996-425). *34th Aerospace Sciences Meeting and Exhibit*, Reno, Nevada.

Nmira, F., Bouffard, A., & Consalvi, J. L. (2023). Flamelet/transported PDF simulations of ethylene/air jet turbulent non-premixed flame using a three-equation PAH-based soot production model. *Combustion Theory and Modelling*, *27*(6), 820–851

Panchal, A., & Menon, S. (2022). Large eddy simulation of fuel sensitivity in a realistic spray combustor II. Lean blowout analysis. *Combustion and Flame*, *240*, 112161

Patel, N., & Menon, S. (2008). Simulation of spray–turbulence–flame interactions in a lean direct injection combustor. *Combustion and Flame*, *153*(1-2), 228-257

Selvaraj, P., Arias, P. G., Lee, B. J., Im, H. G., Wang, Y., Gao, Y., Park, S., Sarathy, S. M., Lu, T., & Chung, S. H. (2016). A computational study of ethylene–air sooting flames: Effects of large polycyclic aromatic hydrocarbons. *Combustion and Flame*, *163*, 427-436

Slavinskaya, N. A., & Frank, P. (2009). A modelling study of aromatic soot precursors formation in laminar methane and ethene flames. *Combustion and Flame*, *156*(9), 1705-1722

Srinivasan, S., & Menon, S. (2014). Linear eddy mixing model studies of high Karlovitz number turbulent premixed flames.*Flow, turbulence, and combustion*, *93*, 189-219

Wang, H., and Frenklach, M. (1997). A detailed kinetic modeling study of aromatics formation in laminar premixed acetylene and ethylene flames. *Combustion Flame, 110*(1–2), 173–221

Wang, H., Xu, R., Wang, K., Bowman, C. T., Hanson, R. K., Davidson, D. F., Brezinsky, K. and Egolfopoulos, F. N. (2018) A physics-based approach to modeling real-fuel combustion chemistry-I. Evidence from experiments, and thermodynamic, chemical kinetic and statistical considerations *Combustion and Flame, 193,* 502-519